DESIGN AND PROTOTYPE DEVELOPMENT OF MOTION AND SHOCK SENSING RF TAGS

A Thesis
Presented to
The Academic Faculty

by

Muhammad Bashir Akbar

In Partial Fulfillment
of the Requirements for the Degree
Master of Science in the
School of Electrical and Computer Engineering

Georgia Institute of Technology
May 2012

DESIGN AND PROTOTYPE DEVELOPMENT OF MOTION AND SHOCK SENSING RF TAGS

Approved by:

Professor Gregory D. Durgin, Advisor
School of Electrical and Computer Engineering
Georgia Institute of Technology

Professor Andrew F. Peterson
School of Electrical and Computer Engineering
Georgia Institute of Technology

Professor David G. Taylor
School of Electrical and Computer Engineering
Georgia Institute of Technology

Date Approved: March 28, 2012

This thesis is dedicated

To my parents, Ali Akbar and Farooqa,and my Siblings,

Saleem, Jamil, Naeem, Saeed, Munir and Shamaila.

For believing in me.

ACKNOWLEDGEMENTS

I want to thank my sponsors for giving me an extraordinary opportunity to study at the Georgia Institute of Technology. I am deeply indebted to my advisor, Dr Gregory D. Durgin for his guidance, wisdom, patience, goodwill and help at every step. I express my deep gratitude to him. I am extremely grateful to my committee, Dr Andrew F. Peterson, Dr David G. Taylor for their time, helpful comments and valuable feedback. I owe a great deal of thanks to the Propagation Group student members, Azhar, Chris, Marcin, Koo, Trotter and Blake for their support and assistance throughout my work.

A humble word of thanks to my parents for their prayers, affection, continuous guidance and support, without them I would not be at the place where I am. In addition, I am grateful to all my siblings for believing in me. In the end, I sincerely thank Almighty Allah for bestowing endless blessings on me.

TABLE OF CONTENTS

LIST OF TABLES

LIST OF FIGURES

SUMMARY

Since the inception of the backscatter-radio technology, this field has continually evolved. As a result, this technology is used for a multitude of applications like personnel identification, logistics and assets management and military purposes etc. Radio Frequency Identification (RFID) technology works in several ISM-frequency bands. This work pertains to the design and development of an RF tag that uses 5.8 GHz ISM band for backscatter. This frequency band has many inherent advantages like higher gain antennas, smaller sized tags, increased immunity to conductive object losses, and larger RF bandwidth.

The objective of this research is design and prototype development of an RF tag capable of sensing acceleration, angular motion, and shock experienced by an object on which it is installed. The sensed information is modulated onto an incident continuous wave (CW) and backscattered to the reader. Literature research suggested that such work has not been done previously using an RFID platform. The challenges include integration of the sensor, antenna and other electronics to efficiently backscatter the information to the receiver, designing a suitable planar antenna, real-time backscattering of the sensed information, and low power consumption. As a further step, it is required to design and integrate two antennas on RF tag to simultaneously backscatter the same information; and to measure and compare its effect with single antenna tag.

The sensed impact/shock and rotational movement information from the inertial sensors (accelerometer and gyroscope) was backscattered instantly and displayed on the custom developed graphical user interface. The development of GUI was not part of this project and was developed by another lab member. RF Tags with single

and dual antenna configurations were designed and tested. It was observed that by increasing the number of antennas higher read range can be achieved. Moreover, by doubling the antennas the radar cross-section for the tag was approximately doubled.

CHAPTER I

INTRODUCTION

Radio frequency identification (RFID) is a rapidly developing, automatic wireless data collection and object identification technology with a long history. In recent years, this has become a necessity in many fields to provide information about the tagged objects. The information can be of any type, ranging from simple object serial number to more intricate applications like object tracking using complex combination of information from the tag.

Several methods have been in place for decades to identify the objects. Each method has its own trade-offs, and varying based on its application. Common examples are enumerated below [2]:

1: Barcode system.

2: Optical character recognition.

3: Biometric systems.

4: RF Smart cards.

5: RFID systems.

1.1 RFID Systems

An RFID system is a contact-less identification system whose system configuration varies from conventional radio systems. It brings together concepts and elements from extremely varied fields: RF technology, data security (encryption), wireless communication, radio and radar engineering, semiconductors, manufacturing technology, etc.

1.1.1 RFID Systems: Strengths and Weakness

Following is a small list highlighting strengths and weakness depicting that RFID systems have [2]:

1: Higher data capacity.

2: Full duplex, half duplex and sequential communication.

3: Data that can be instantly read from the RF tags.

4: Resistance to unauthorized access.

5: Contact-less communication. Data can be read in both line-of-sight (LOS) and non-light-of-sight (NLOS) cases.

6: Low operational cost.

7: Unlimited applications

In RFID systems the transceiver is commonly referred to as the *reader*. The reader transmits the continuous electromagnetic waves at operating frequency towards the tag, which in turn modulates these wave and reflects them back to the reader's receiver. The reflection of the data from the tag is known as *backscattering*. In some cases, the continuous wave (CW) signals from the reader also provide power to the tag electronics through tag's on-board *charge pump* circuitry, a rectifier constructed using diodes and capacitors, these type of tags are called *passive tags*. However, if the tag is powered-up using a battery, then it falls under the category of *semi-passive* or *battery-assisted* tag. A generic block diagram of the RFID system is shown in Figure 1.

In essence, a backscatter radio retrieves the information from an RF tag by illuminating the device with RF frequency power and demodulating the received signal backscattered from the tag. RF tags have no RF components such as mixers, low noise

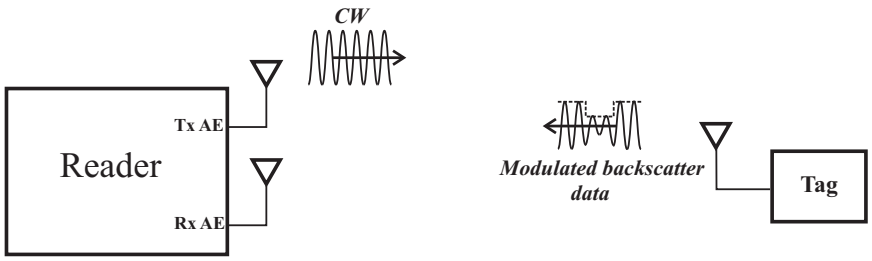

Figure 1: Block diagram of a generic backscatter system.

amplifiers, or filters. It is conventionally a low power consuming device. *Readers*, on the other hand, consist of a coherent oscillator and direct-down conversion receiver, a unique feature of RFID systems that can help in extracting change in phase from pulse to pulse. The transmitted power is within specified Federal Communication Commission (FCC) regulations.

1.1.2 RFID Systems: Frequency Band Classification

The frequency of operation of RFID systems varies throughout the world and typically falls in Industrial, Scientific and Medical (ISM) frequency bands [3, 4]. Although the ISM band has many divisions but not all are used for RFID communication. In the United States, these are typically operated in ISM bands summarized at Table 1 along with generic classification and band names.

Table 1: Industrial, Scientific and Medical (ISM) frequency bands used for RFID systems

Classification	Generic Frequency Band	ISM Frequency Allocation
Low Frequency (LF)	30–300KHz	125–134KHz
High Frequency (HF)	3–30MHz	13.553–13.556MHz
Ultra High Frequency (UHF)	300–3000MHz	860–930MHz
Ultra High Frequency (UHF)	300-3000MHz	2400–2483.5MHz
Super High Frequency (SHF)	3000-30,000MHz	5725–5850MHz

RFID systems that use ISM frequencies in LF and HF bands operate using inductive coupling. By contrast, microwave systems in the frequency range 2.45-5.8 GHz

are coupled using electromagnetic fields [2]. This thesis work deals with development of a prototype RF tag at the last ISM band mentioned in the table above, typically at 5.8 GHz that uses electromagnetic fields.

1.1.3 RFID Systems: Benefits at 5.8 GHz ISM band

Little attention has been given to RFID systems at 5.8 GHz, therefore, automatic traffic toll registration in the 5725–5850 MHz ISM band is the only known commercial RFID application. However, due to smaller wavelength, this range has some inherent benefits for RFID applications, a few of which are listed below:

1: 5.8 GHz antennas are nearly 15% the size of an antenna at 900 MHz. Thus, not only does it reduce the tag footprint but multiple antennas at 5.8 GHz can also fit within the same footprint as a UHF tag with a single antenna [5].

2: For a constant effective antenna aperture (A_{eff}), higher antenna gains (G) are possible due to smaller wavelengths, given by equation (1).

$$G = \frac{4\pi}{\lambda^2} A_{eff} \tag{1}$$

3: Resistant to conductive object degradation [6].

4: Availability of higher RF bandwidth [6].

5: Spatial signal diversity [7].

6: Smaller tag footprints [6].

1.2 Motivation: Shock and motion measurement using RF tags

Head injuries, including concussions, particularly in the game of American football and hockey, have become a subject of deep concern, study and even Congressional debates and hearings in the United States for legislation on concussion [8]. Contrary

to popular belief, a concussion is not a bruise to the brain caused by hitting a hard surface. But it's a violent shaking of the brain inside the skull. Generally, no physical swelling or bleeding is seen on radiological scans. The injury generally occurs when the head either accelerates rapidly and then is stopped, or is spun rapidly. It can lead to serious consequences related to health that can ruin life. Concussions are not limited to brain or head injuries but a severe blow to the jaw can also travel to base of the brain.

Several studies have been conducted by leading sports medical researchers, universities and other institutions on the effects of concussions and ways to avoid them. These studies and concerns have ushered in the development of helmets that prevent / mitigate the impact and lessen the chances of injuries. Few helmet products are developed to measure and record the shock experienced in a head impact, which can later be analyzed [9]. The recorded data is also used to keep track of the number of hard head hits players receive over the course of the season. Some helmet products also include a concussion indicator in their chinstrap that warns the player of a concussion after a hard hit [10]. Very little effort has been put in to measure both the impact of shock or traumatic force to the head and jaw; and by the amount the head and jaw has spun due to a severe blow. There is also no provision of live monitoring and measurement of shock and the resultant degrees of spin.

The aforementioned reasons motivate the development of an RF tag that can instantly *detect, measure and backscatter* the magnitude of shock and degree of spin experienced by the head / jaw or any tagged object on impact.

1.3 Research Overview

The research in this thesis attempts to design a backscatter radio system with the main focus on an RF tag capable of instant *detection, measurement and backscatter* of the *motion, shock and spin* of the tagged object. The major goals are omni-directional

azimuthal coverage, low power consumption, higher bit rates, to backscatter more data packets per second such that no shock or spin experienced by the tagged object is missed, and most of all to design all elements of the tag in a single plane for easy installation. Chapter 2 presents in detail the theory of each module of the tag, the tag design, and its hardware description. It also explains the Georgia Tech Motion ($GTM1.0$) protocol and a general framework of the reader's receiver architecture. Chapter 3 discusses the antenna design, simulation and measured results. Chapter 4 encompasses the future work followed by a conclusion in chapter 5.

CHAPTER II

THEORY, OPERATION AND DESIGN

2.1 Background

The RF tag sensor described in this chapter is fundamentally different from the resonance–shifting technique used with inductively coupled sensors in [11]. The resonance–shifting technique relies on a controlled environment and calibration procedure where a resonance shift corresponds with a change in chemical concentration. The following work more closely follows the WISP platform in [12] where digital or analog sensors are sampled by a microcontroller and then digitally modulated back to a reader. However, the following work uses the 5.8 GHz ISM band for transmission which has numerous benefits as listed in chapter 1. Furthermore, this system does not rely on the EPC Global Gen 2 communication standard and can use custom communication protocols which can more efficiently reflect data to the reader.

Reduction of tag size is a key aspect in this application. High frequency backscatter systems have an inherent advantage of smaller wavelengths resulting in small antennas and thin microstrip lines; thus, their tag form factors tend to be smaller than their UHF counter parts. RF tags modulate and reflect the incident continuous wave (CW) RF energy, by using a *load modulation technique, i.e.* modulating the antenna between different loads. Traditionally, a binary modulation scheme is used but a higher state modulation scheme can also be used [13]. The modulation factor M, is given by [14]

$$M = \frac{1}{4} \left| \Gamma_A \; - \; \Gamma_B \right|^2 \tag{2}$$

where the reflection co-efficient, Γ_{AB}, is defined as [5]

$$\Gamma_{A,B} = \frac{Z_{A,B} - Z^*_{ant}}{Z_{A,B} + Z_{ant}} \tag{3}$$

2.2 Basic Tag Description

The RF tag senses 3–axis rotations and 3–dimensional acceleration of the tagged object. Motion and shock sensing is done using Micro-Electro-Mechanical Systems (MEMS) technology based sensors. The sensor portion consists of the Analog Devices, ADXL–345, 3–axis digital MEMS Accelerometer capable of measuring up to $\pm 16g$ shock values [15] and an InvenSense, IMU–3000, Motion Processing Unit (MPU). The MPU is capable of 6-axis sensor fusion with an embedded 3–axis digital MEMS Gyroscope and Digital Motion Processor (DMP) [16]. Once programmed, the MPU can automatically access an external third party accelerometer and can add its own gyroscope measurements and noise filtering to the data using the embedded DMP. However, this feature has not been used in the current work. The IMU–3000's embedded Gyroscope is capable of measuring up-to ± 2000 degrees per sec (dps). Although in practical scenarios the magnitude of impact and rate of resulting twist may be higher than the sensor measurement limits used in this design, however, it must be kept in mind that this work only pertains to prototype development for proof of concept purposes. The accelerometer measures both the dynamic acceleration resulting from motion or shock and static acceleration, such as gravity. Both the MEMS sensors are low power consuming devices. A summary of the sensors specification is listed in Table 2. Further details can be found in [15, 16].

Table 2: Summary of Sensors Specification. ADXL–345 and IMU–3000

Sensor	Part No	Programmable Limits	Units	Voltage&Current
Accelerometer	ADXL–345	±2g,±4,±8,±16	g	3.3V,150uA
Gyroscope	IMU–3000	±250,±500,±1000±2000	deg/sec	3.3V,6mA

The Texas Instrument's ultra low-power microcontroller, MSP430F2619 was used

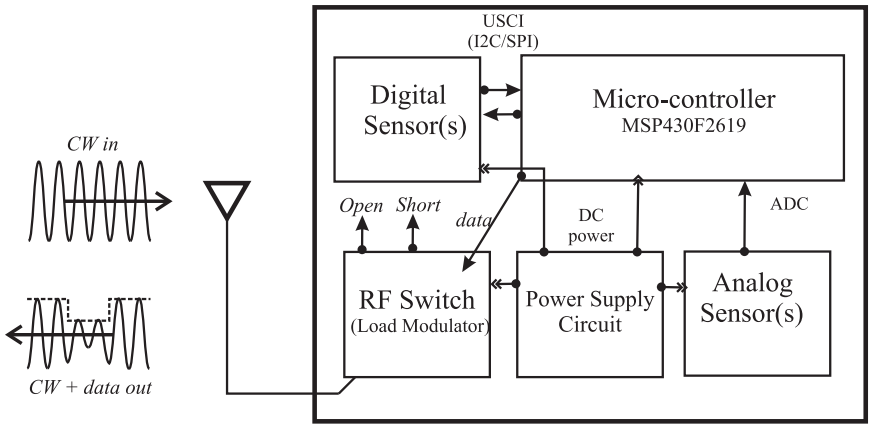

Figure 2: Detailed block diagram of a generic backscatter RF tag. Texas Instrument's TI-MSP430F2619 microcontroller acquires the sensor data using USCI interface or on-board analog to digital converters. The tag data is backscattered by modulating it over the incident continuous wave signal.

as the micro-controller unit (MCU). The MCU samples the data from the digital sensors using the universal serial communication interface (USCI), I^2C mode. The sampled data is statistically *whitened*, and encoded using Manchester Encoding, processed to calculate cyclic redundancy check (CRC), and backscattered using Mini-circuits' absorptive GaAsFETs RF switch. The RF switch is controlled using USCI, serial peripheral interface (SPI) mode. The tag is a battery-assisted, semi-passive device that operates on 3.3 VDC, 225 mAh coin battery cell with a current consumption of 17 mA. A detailed block diagram of the RF tag is given in Figure 2.

2.2.1 Theory of operation: Accelerometer

The Analog Devices' ADXL–345 is a 3–axis accelerometer that can measure both dynamic acceleration resulting from impacts/motion and static acceleration, such as gravity. It has a programmable measurement range as given in Table 2. ADXL–345 can be programmed and data can be offloaded through both UCSI, I^2C and SPI modes, however, this work only used I^2C mode to transfer the data between MCU and the sensors; and measures the acceleration by measuring the differential

capacitance between MEMS structures inside the IC. The measured data is quantized and stored in the two's complement form in six bytes with two bytes for each axis. Depending on the selected resolution ($\pm 2g$, $\pm 4g$, $\pm 8g$,or $\pm 16g$) some of the bits in the most significant byte of the axis data output are reserved for the sign bits. The alignment of the registers and the number of bits required to be read for each axis depend upon the selected g-value and is given in the data formatting section of the data sheet. For the case of $\pm 16g$ or a $32g$ range in full resolution mode, the upper nibble in the most significant byte is for the sign of the measured acceleration. By converting the register values (which are in two's complement) into decimal/integer form and multiplying it by the scaling factor of 3.9 mg (for full resolution), we can get the acceleration along a desired axis in g's. This is given in equation (4),

$$\|\vec{a}_{x,y,z}\| = (\text{Integer value of 2's complement}) * S_a \tag{4}$$

where $\|\vec{a}_{x,y,z}\|$ is the magnitude of the acceleration along any Cartesian axis (with respect to device) in g's and S_a is the scaling factor that can be calculated using equation (5).

$$S_a = \frac{Total\ scale\ range\ in\ g}{2^{Number\ of\ resolution\ bits}} \tag{5}$$

For example, for the case of ± 16 g or a 32 g range with 13-bit resolution, the S_a can be calculated as follows:

$$S_a = \frac{32}{2^{13}} = 3.90625\ mg \tag{6}$$

The number of bits for $\pm 2g$, $\pm 4g$, $\pm 8g$ and $\pm 16g$ in full resolution are 10, 11, 12, and 13–bits, respectively, so that a different scale factor is used for each g–scale value; however, the datasheet suggests to use a scale factor of 3.90625 mg for all g-values in full resolution. Besides measuring the dynamic acceleration, the accelerometer

can also be used for tilt sensing, single/double tap detection, free-fall detection and activity/inactivity monitoring. The details in this section were summarized from [15].

2.2.2 Theory of operation: Gyroscope

InvenSense, IMU-3000, has an embedded 3–axis digital MEMS gyroscope package that works on the principle of the Coriolis Effect. It contains three independent gyroscopes, one for each axis which when rotated around sensed axis the Coriolis Effect causes a vibration which is measured as differential capacitance. It can be programmed to measure any of the rotation rate options given in Table 2. A slave third–party accelerometer can also be connected with the IMU-3000 which can automatically download the acceleration values and process data through the embedded DMP. However, this option has not been used in this work. The gyroscope can be programmed and sensed data can be read using the USCI, I^2C protocol. The output values are stored in two's complement form in six bytes with two bytes (higher byte and lower byte) for each axis. Unlike the accelerometer, only the most significant bit of the higher byte is the sign bit and the decimal value of the $2's$ complement data can then be multiplied by a scale factor to get the exact gyro value in *degrees per sec*. This is given in equation (7).

$$\|\vec{\omega}_{x,y,z}\| = (\text{Integer value of 2's complement}) * S_g \tag{7}$$

where $\|\vec{\omega}_{x,y,z}\|$ is the magnitude of the gyro-rotation along any Cartesian axis (with respect to device) in *degrees per sec* and S_g is the gyro scaling factor that can be calculated using equation (8).

$$S_g = \frac{Total\ scale\ range\ in\ degrees\ per\ sec}{2^{Number\ of\ resolution\ bits}} \tag{8}$$

For example, for the case of ± 2000 *degrees per sec* or a 4000 *degrees per sec* range with 16-bit word the S_g can be calculated as follows:

$$S_g = \frac{4000}{2^{16}} = 0.0610352 \ degrees \ per \ sec \tag{9}$$

The details in this section were summarized from [16].

2.2.3 Differential Binary Phase Shift Keying

Phase shift keying (PSK) is the digital modulation technique that modulates the carrier wave by varying its phase. These phase changes are encoded in a finite number of bits, and each combination of bits is known as a *symbol* which *symbolizes* a particular phase. An M-ary PSK signal can be written as [17]

$$\tilde{s}(t) = A \sum nb(t - nT, \mathbf{x}_n) \tag{10}$$

where A is the magnitude of the signal and

$$b(t, \mathbf{x}_n) = h_a(t) \exp(j\theta_n) \tag{11}$$

where $h_a(t)$ is the amplitude shaping pulse, and θ_n is the excess phase that takes on the following values,

$$\theta_n = \frac{2\pi}{M}\mathbf{x}_n \tag{12}$$

where symbols $\mathbf{x}_n \in$ 0,1,...,M-1.

Binary phase shift keying (BPSK) is the simplest of the M-ary PSK schemes with M=2 which implies symbols $\mathbf{x}_n \in$ 0,1. From equation(12), the two excess phases are 0° (represented by '0') and 180° (represented by '1'), this means that the two signals are always 180° apart. M-ary PSK signals are generally shown using a *signal space diagram* also known as a *constellation diagram*, such a diagram for BPSK is shown in Figure 3.

The phase of the received PSK signal is given by [17]

$$\theta_k = \frac{2\pi}{M}x_k + \phi \tag{13}$$

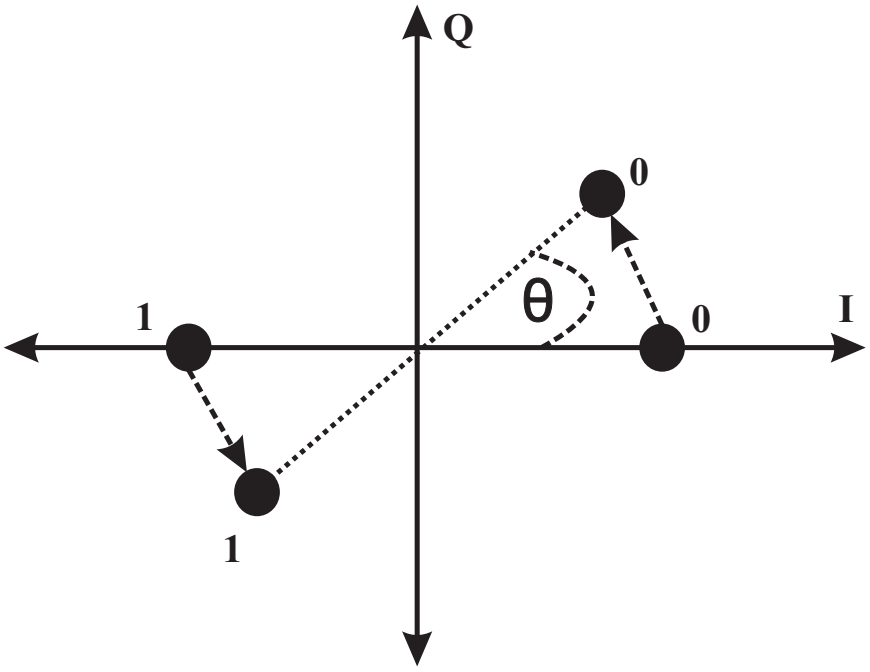

Figure 3: Signal space diagram of BPSK modulation scheme that consists of two symbols '0' and '1'. Both the symbols are always 180° apart no matter what is the phase of the signal, θ, in the signal space diagram.

where ϕ is the random phase added by the channel which can be adjusted by the receiver by adding a product term of $\exp(-j\phi)$. However, this is not a simple operation because the symmetries in the signal space can lead to *phase ambiguity*, i.e. any phase incorporated by the channel can take the form of $\phi + 2k\pi/M$, with k as an integer, and will create a replica of same set of phases in the constellation. This can disrupt the phase of the signal. Also, from equation (13), it can cause synchronization problems if there is a series of bits that translates to the same phase shift over and over again. To recover the information correctly, these ambiguities in phase must be resolved.

Differential encoding is the typical scheme that is used to compensate for $2k\pi/M$ phase ambiguities. In differential encoded PSK, the bit sequence represents the relative phase, or phase transition between the adjacent symbols. The original information sequence is differential encoded using equation (14) into the new sequence [18].

$$y[n] = y[n-1] \oplus x[n] \tag{14}$$

where x[n] is the input binary sequence, y[n] is the differential binary encoded sequence, n is an integer and $\oplus$ is the modulo-M addition. M = 2 is the case of BPSK.

2.2.4 Manchester Coding

In order to remove the DC offset in the amplifiers and comparators, the conventional receivers couple the data using a series capacitor. The size(value) of the series capacitor is determined depending on the maximum length of continuous 1s or 0s in the received data. A detection error can easily be caused by not choosing the proper value of the capacitor. The data will begin to decay or droop if a very small size of capacitor is picked to remove the DC component. In contrast, choosing a very large value of the series capacitor results in a longer time to charge the capacitor to

the steady state condition, thereby more time is needed by the receiver to properly decode the bit sequence. The Manchester coding (MC) is one of the schemes that can be used to resolve this anomaly by using a DC balanced pulse shape. By DC balanced it is meant that a binary '1' is represented as binary '10' and a binary '0' is represented as binary '01' in such a way that the transition in their pulse shape is equally spaced in period of time, i.e. a binary '1' has positive voltage during the first half of the bit period and a negative voltage during the second half of the bit period, vice-versa is true for binary '0'. The pulse shape for a Manchester coded binary '1' and '0' is given in Figure 4. The MC ensures a transition occurs in the middle of each bit (or symbol) period $T_\circ$.

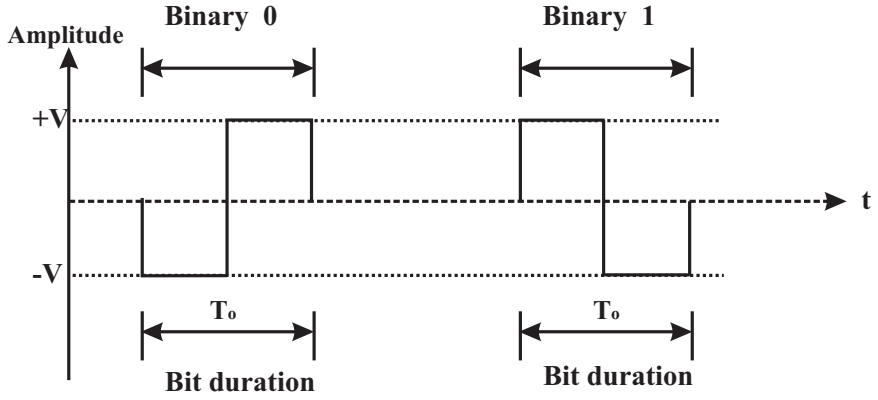

Figure 4: Pulse shape for Manchester coded binary '0' and binary '1', with a bit duration of $T_\circ$ and amplitude, $\pm V$. A binary '0' is represented by a pulse that has a negative voltage during the first half of the bit duration and a positive during the remaining half of the bit duration. A binary '1' is represented by a pulse that has a positive voltage during the first half of the bit duration and a negative voltage during the remaining half of the bit duration. A transition in the middle of the bit duration helps in adjusting the receiver's clock.

Manchester coding (MC), also known as "*split phase*" or "*digital bi-phase*", has a signal constellation identical to the BPSK signal given in Figure 3. The basis function

of the MC is given by [19]:

$$\varphi(t) = \begin{cases} \frac{1}{\sqrt{T}} & 0 \leq t \leq \frac{T}{2} \\ -\frac{1}{\sqrt{T}} & \frac{T}{2} \leq t \leq T \\ 0 & elsewhere \end{cases} \tag{15}$$

The power spectral density (PSD) of MC is the Fourier transform of the MC pulse which is a product of a sinc function and a sine function with zero crossings equally spaced at $\frac{2}{T_\circ}$ Hz. The PSD is given by the following equation [20]:

$$S(f) = V^2 T_\circ \left[\frac{\sin\left(\frac{\omega T_\circ}{4}\right)}{\frac{\omega T_\circ}{4}}\right]^2 \left[\sin\left(\frac{\omega T_\circ}{4}\right)\right]^2 \tag{16}$$

where $\pm V$ is the positive/negative voltage of the MC pulse, $T_\circ$ is the bit period and ω is the radian frequency. A normalized PSD of the MC was plotted in MatLab for a bit period $T_\circ$ of 2 microseconds and is given in Figure 5.

2.2.5 Cyclic Redundancy Check

Cyclic Redundancy Check (CRC) is an algorithmic based *cyclic* procedure used in digital networks and devices to detect unintentional changes in bits of raw data block (raw information). It is a data verification routine / operation which is *redundant* to the desired information and is calculated using a cyclic code in which desired information is divided by a standard polynomial called the *generator polynomial* to find the remainder of this division process, also called as the *check value*. The *check value*, referred to as an *n-bit* check value or CRC, has a fixed length which is always less than the length of the generator polynomial. The computed CRC is appended to the desired data block and transmitted over the channel. On the receiver side the same cyclic procedure using the same generator polynomial divisor is repeated to compute the CRC of the desired data block only and is compared to the received CRC value. If the two CRC's match then the data is considered as error free and processed, otherwise the received block contains data error. In the case of an error,

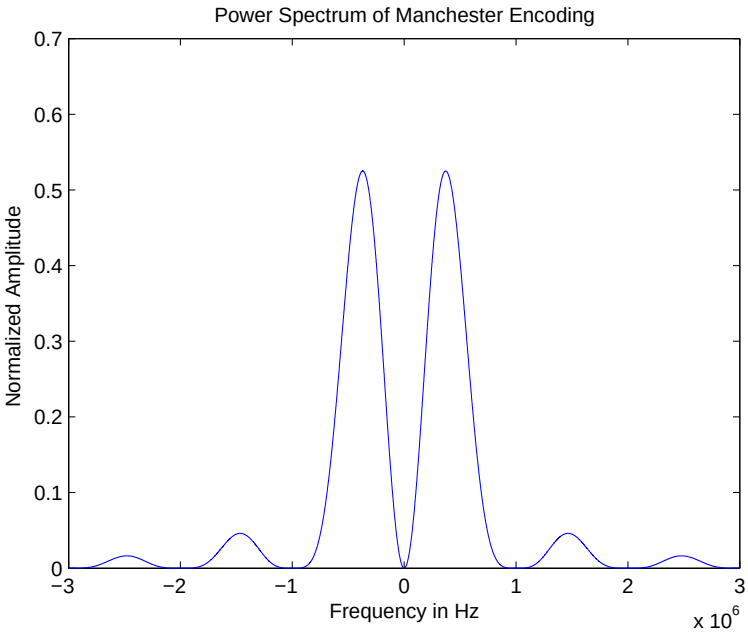

Figure 5: The normalized power spectral density (PSD) of the Manchester coded waveform for a bit period $T_\circ$ of 2 microseconds depicting a DC balanced sinc waveform with no DC component at baseband. The zero crossings of the PSD are equally spaced at $\frac{2}{T}$ Hz

the receiver can take remedial steps such as dropping the error packet, rereading, or requesting the data block again, etc. The generator polynomial is determined by the co-efficients of standard polynomials. In this work, we used a CRC–8 (Dallas/Maxim) polynomial $x^8 + x^5 + x^4 + 1$ represented in reversed format as the hexadecimal value $0\mathbf{x}8C$.

2.3 Theory of operation: RF Tag

A block diagram of the semi-passive microwave RFID enabled sensor integrated with a partitioned loop antenna is shown in Figure 2 along with a photo of the prototype RF tag in Figure 6. A Texas Instruments ultra-low power MSP430F2619 microcontroller acquires sensor output, packetizes the data, and modulates the packet data onto the incident CW via an RF switch. Desired sensor data can be acquired from sensors via

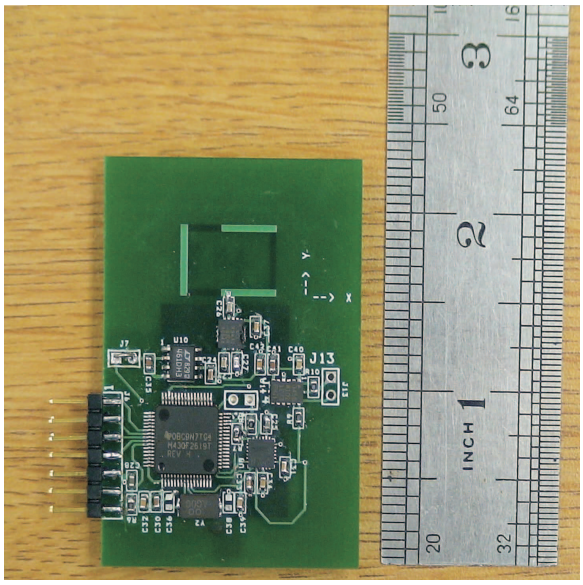

Figure 6: Image of single antenna RF sensor tag. The tag is battery assisted, semi–passive tag that operates on 3.3 VDC, 225 mAh coin cell battery with 16 mA current consumption. The tag backscatters the data by toggling the RF switch installed at the antenna feed point.

a digital universal serial communication interface (USCI) or built-in analog to digital converter (ADC) [21]. Data communication speed depends upon the upper limit of the internal/external digital clock of the controller. In this design, data is acquired using the USCI, I^2C interface and an external clock source of 10 MHz was used.

2.3.1 Georgia Tech Motion Protocol

Instead of using any of the standardized data packets defined for wireless sensor networks (WSNs), a customized packet is designed in this work. The packet is eighteen bytes long which consists of three header/preamble bytes, two tag ID bytes, twelve bytes sensors' acquired data, and one computed CRC-value byte. The arrangement of the packet is shown in Figure 7.

The benefits of choosing Manchester coding have been discussed in section 2.2.4. A flow chart of the Georgia Tech Motion Protocol 1.0 (GTM 1.0) is given in Figure 8 and summarized below:

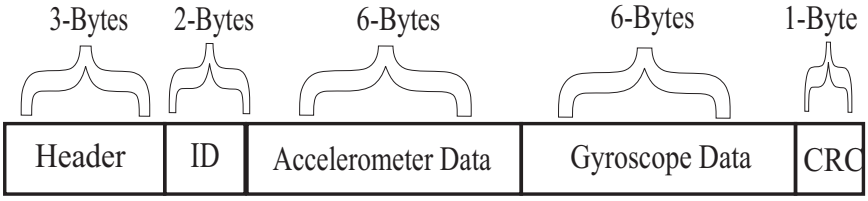

Figure 7: Packet composition of Georgia Tech Motion Protocol 1.0 (GTM 1.0). A single packet is composed of eighteen bytes with bytes distribution as highlighted in the figure.

1: The microcontroller, MSP430F2619, is intiallized by configuring the I/O port directions, selecting its primary or secondary function, setting up the external clock frequency and checking clock-status.

2: At second step, all the peripheral sensor modules are initialized to custom settings to acquire the particular range of data at desired sensors's sensitivity.

3: The data from gyroscope and accelerometer is read from the I^2C interface and stored as bytes in buffers. A total of twelve data bytes are received from the inertial sensors (six-bytes from each sensor).

4: The CRC value is computed and appended to the data.

5: All the data bytes are arranged in an eighteen byte data packet as shown in Figure 7 and the entire packet is digitally encoded using Manchester encoding scheme. This also automatically *whitens* each data byte.

6: The resulting bit sequence from the above step is backscattered by load modulating the RF switch between open and short loads.

7: The process from step (3) to (7) is repeated continually.

The RF switch is connected to the feed point of a partitioned loop antenna through a DC blocking capacitor. The switch is controlled via the data-output pin of the microcontroller's USCI, SPI interface that alternates the antennas load between a short

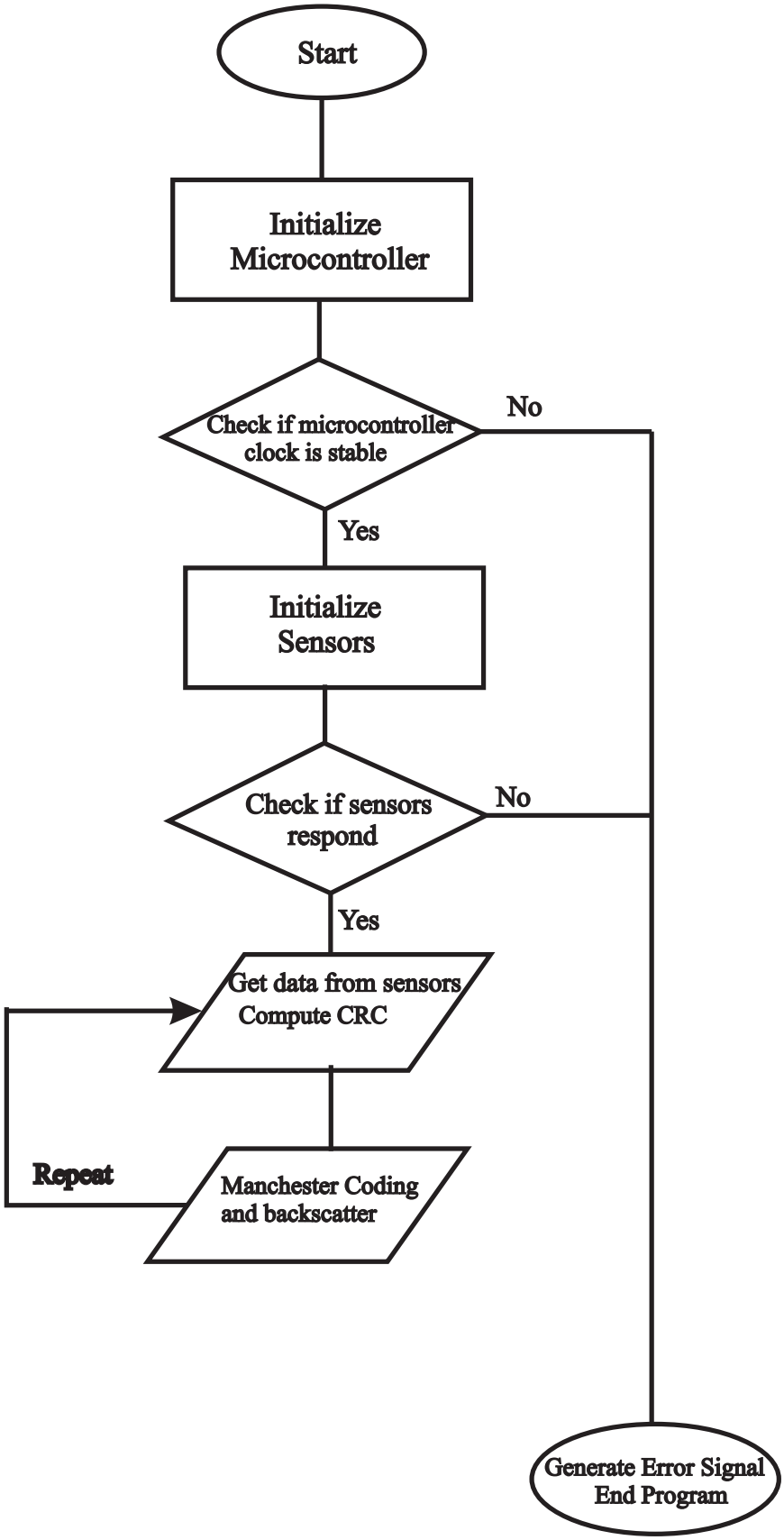

Figure 8: Complete flowchart of Georgia Tech Motion Protocol 1.0 (GTM 1.0).

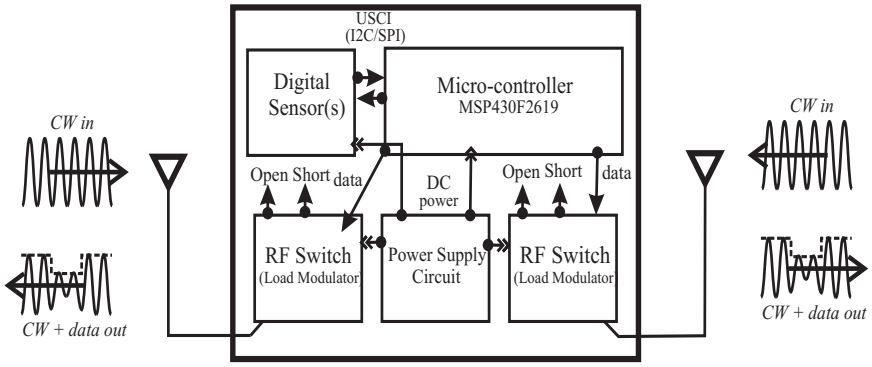

Figure 9: Block diagram of a dual antenna tag. The RF switches for both the antennas are controlled via single control line from microcontroller.

and open circuit, enabling Manchester encoded binary phase shift keying (BPSK) modulation via a change in backscattered signal. All RF traces are 50 Ω electrically short microstrip lines.

2.3.2 Dual Antenna RF Tag

A similar tag, as described above, with two identical partitioned loop antennas was also designed to test the increase in the tag's read range and its radar cross-section due to multiple antennas. The details and results will be discussed in the next chapter. The block diagram of the multiple antenna tag is shown in Figure 9 and the image of the dual antenna alongside the single antenna tag is given in Figure 10. The theory of tag operation, sensor modules, and motion protocol is identical to the single antenna tag protocol described above. However, both antennas have their own RF switches which are toggled simultaneously by a single control line from the microcontroller.

2.4 Reader: Backscatter Radio Transceiver

The transceiver block diagram is shown in Figure 11. The transceiver is set up in a bi-static configuration where two antennas are used, one for transmitting and one for receiving. This configuration minimizes coupling of the high-power RF into the receive chain. On the transmitter side, a 5.8 GHz carrier wave provided by a local

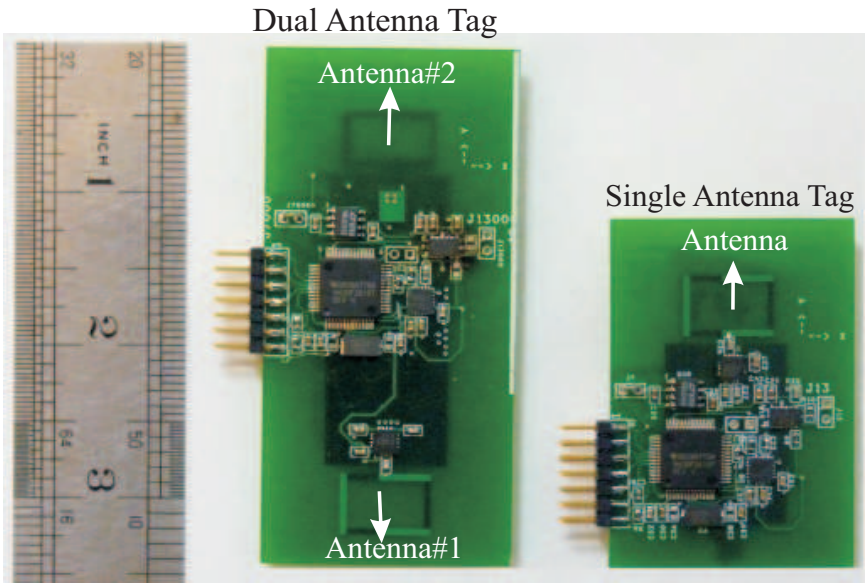

Figure 10: Microwave backscatter sensor tags. the dual antenna tag is in the center and the single antenna tag is on the right). Both the antennas on the dual antenna tag, face 180° in opposite directions and are fabricated on different layers of the FR406 4–layer board. (Reprinted from [1] © 2012 IEEE)

oscillator is amplified and transmitted by an antenna. The receiver uses a coherent homodyne or direct down-conversion topology. This design provides cancellation of the strong self-interference received by the system. This fact is very important as the modulated backscatter signal from the tag will be much weaker than the un-modulated, self-interference signals received by the reader.

The received signal follows the path outlined in Figure 11. First, the received RF passes through a band pass filter before being amplified by a low-noise amplifier. This signal is then split and mixed down to in-phase (I) and quadrature (Q) baseband. The resulting signals are low-pass filtered to remove inter-modulation products and are sent through a DC-blocking capacitor to remove any large DC components. Finally, both the I and Q signals pass through a variable gain amplifier and low-pass filter before being amplified again at baseband (not shown in figure). These two signals are then sampled by a USRP N200 software defined radio (SDR) for baseband processing.

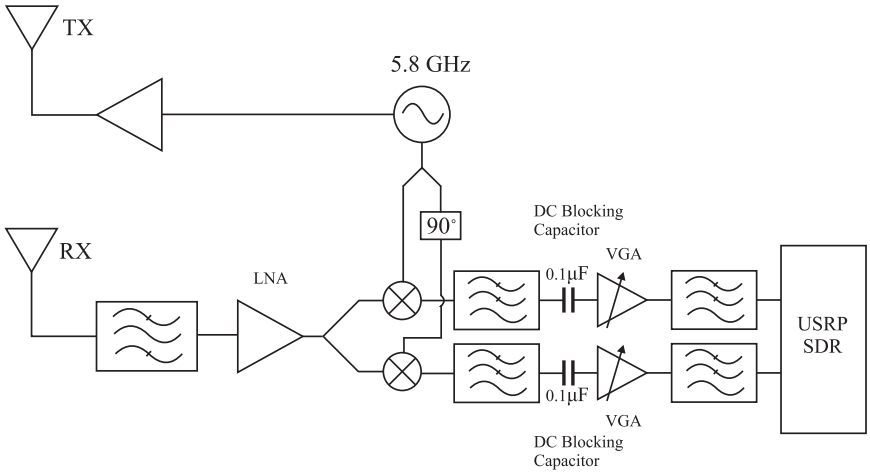

Figure 11: Diagram of the 5.8 GHz backscatter radio transceiver. The transmit chain simply amplifies the 5.8 GHz carrier wave. The receive chain uses a homodyne receiver architecture whose in-phase and quadrature outputs are sampled by a USRP software defined radio (SDR) for baseband processing.

This receiver operates in the entire 5725-5850 MHz ISM band and can tolerate a maximum input power of -12 dBm in bi-static configuration.

2.5 Summary

This chapter documented the theoretical description of single and dual antenna tags designed to measure shock and motion of the tagged object. The working principle and operation of each of its sub-modules was also presented. The Georgia Tech Motion protocol 1.0 (GTM 1.0) developed for wireless backscatter communication to relay back inertial data to the reader unit was explained. GTM 1.0 is optimized for low power consumption, high-speed, low-latency transfer of digital sensor data. Future versions of the protocol can be further optimized for long read range, capable of measuring higher shocks/impacts and higher rotational rates. The current performance specifications of GTM 1.0 are summarized in Table 3.

Table 3: Summary of performance specifications of GTM–1.0.

System Parameter	Value	Remarks
Max measurable shock	$16gs$	Maximum limit of accelerometer used
Max measurable rotation	2000 *degree per sec*	Maximum limit of gyroscope used
Packet rate	200 *packets per sec*	–
Header	3–bytes	Figure 7
Tag–ID	2–bytes	Figure 7
Inertial data	12-bytes	Figure 7
Checksum	8–bit	Figure 7
Sensor power draw	$\lessapprox$ 57 mW	3.3 VDC, 17 mA
Backscatter frequency	5.725-5.850 GHz	–

CHAPTER III

SQUARE LOOP ANTENNA : THEORY DESIGN AND TESTING

3.1 Introduction

Any metallic device used to radiate or receive electromagnetic waves can be antenna. The antennas can be of many different structures and shapes depending upon application and frequency and can be fabricated on substrate materials in the form of patch or strip line. A loop antenna is a simple antenna with versatile applications that can be easily implemented and built in many shapes. The popularity of loop antennas among engineers stems from its simplicity of design and fabrication, ease of integration, low-cost of manufacture and versatile application. Most common polygonal loop antenna shapes are circular, square, rectangular and rhombic. The fields of loop antennas can be determined by approximating the small loop to be an infinitesimal magnetic dipole with a radiation pattern null orthogonal to the plane of loop. Electrically small loop antennas have small radiation resistance and therefore are often inefficient radiators. For electrically large loop antennas (perimeter approximately greater than or equal to one free space wavelength), the radiation pattern null shifts from the orthogonal plane of the PCB to in-plane with the PCB. This transition is due to large phase variations across the length of the strip line. These variations can be reduced, and total antenna length can be shortened, by dividing the loop into smaller portions and overlapping them to capacitively load the antenna as shown by Hasse et. al in [22]. The capacitance of the overlap area can be found using the relation:

$$C = \frac{\epsilon_\circ \epsilon_r A}{h} \tag{17}$$

where A is the required overlapped area, h is the substrate thickness and C is the required capacitance [22].

An omni-directional pattern is ideally suited for use in RFID enabled sensor systems where the orientation of the sensor cannot be controlled. Hasse implemented a square segmented loop on two layer Rogers RT/Duroid board. This design optimized the overlapping capacitances to achieve an omni-directional antenna and to overcome phase variations, but this design didn't include any effects of RF switches or ground planes. In this work, the same concept was extended to FR-406 4-layer board with a thick inner core. This chapter presents the design, simulation, experimental results of the partitioned square loop antenna. In addition, this chapter also presents an improvement of the read range, radar cross–section (RCS) and reliability of radio frequency identification (RFID) tags using multiple antennas.

3.2 Far Field Expression for Square Loop Antenna

The theoretical analysis of the polygonal loop antenna has been unsuccessful due to their complex structure [23]. However, design curves obtained using the Method of Moments, do exist and can be used for design of polygonal loop antennas for practical applications. Consider a square loop antenna shown in Figure 12. The far fields of a square loop radiator can be approximated using the fields of a linear dipole antenna under the assumption that each of its side is a small linear dipole with length l of constant current $I_\circ$. Then from Figure 12, the far field component of electric field E_ϕ in y-z plane can be written as sum of $E_{\phi 1}$ and $E_{\phi 2}$.

$$E_\phi \;=\; E_{\phi 1} \;+\; E_{\phi 2} \;=\; j\eta \frac{kI_\circ l}{4\pi} \left[\frac{\exp(-jkr_1)}{r_1} \;-\; \frac{\exp(-jkr_2)}{r_2} \right] \tag{18}$$

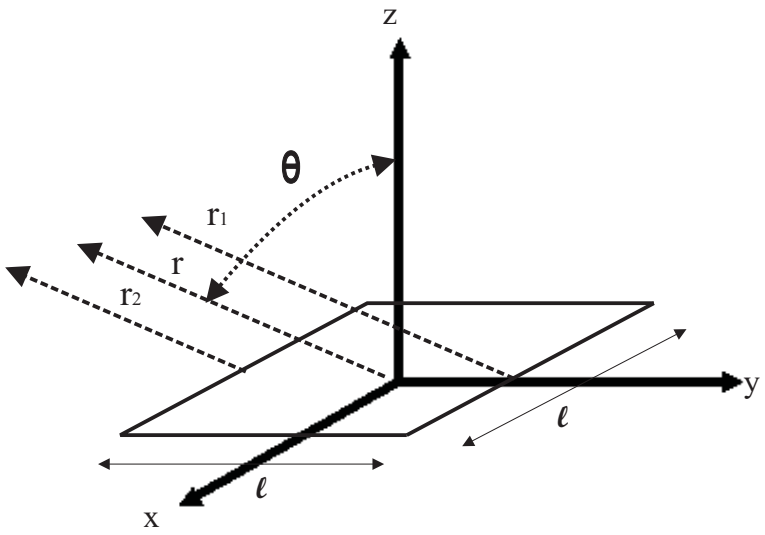

Figure 12: Far field observation for a square loop antenna with constant current $I_\circ$ in counter clockwise direction in Y–Z plane

Since the pattern is omni-directional for each wire element in that plane, we can simplify the r_1 and r_2 for phase and amplitude variations using far field approximation ($kr \gg 1$) as follows:

for phase variations

$$r_1 \backsimeq r + \frac{l}{2}\sin\theta$$
$$r_2 \backsimeq r - \frac{l}{2}\sin\theta$$

for amplitude variations

$$r_1 \backsimeq r_2 \backsimeq r \tag{19}$$

equation (18) can now be written as

$$E_\phi \;=\; \eta\frac{kI_\circ l\exp(-jkr)}{2\pi r}\sin\left(\frac{kl}{2}\sin\theta\right) \tag{20}$$

If l is small ($l \leq \frac{\lambda}{50}$), then equation 20 can be written as

$$E_\phi \;=\; \eta\frac{(kl)^2 I_\circ\exp(-jkr)}{4\pi r}\sin\theta \;=\; \eta\frac{\pi\Delta A I_\circ\exp(-jkr)}{\lambda^2 r}\sin\theta \tag{21}$$

where $\Delta A = l^2$ is the geometrical area of the loop. The corresponding magnetic field is given by

$$H_\theta \;=\; -\frac{E_\phi}{\eta} \;=\; -\frac{\pi\Delta A I_\circ\exp -jkr}{\lambda^2 r}\sin\theta \tag{22}$$

It can be observed that equations (21) and (22) are similar to the far zone field expression for a small circular loop. This is also stated by Smith in Chapter 5 of [24]. Similar expressions can be used for far fields of rectangular loops. Balanis [23] suggests that the fields in the other planes are difficult to obtain. Design curves for other polygonal shape antennas are presented in various books such as [23] which can be used for practical design considerations. This section has been summarized from [23].

3.3 Design of Partitioned Loop Antenna

As mentioned earlier, Hasse in [22] implemented a square segmented loop on two layer Rogers RT/Duroid board. In this work, the same concept was extended to an FR–406 four layer board with a thick inner core. The layer stack-up for the FR–406 62mils board with dimensions is shown in Figure 13. The partitioned loop antenna at 5.8 GHz was designed and simulated using Ansoft's High Frequency Structure Simulator (HFSS) software. It was fabricated on the top two layers of the 4-layer printed circuit board board. The RF switch was installed at the feed point of the partitioned loop antenna through a DC blocking capacitor.

The FR-406 is a high performance epoxy laminate material that is inserted between two layers of prepreg-2116 which is resin-impregnated woven fiberglass. Its low

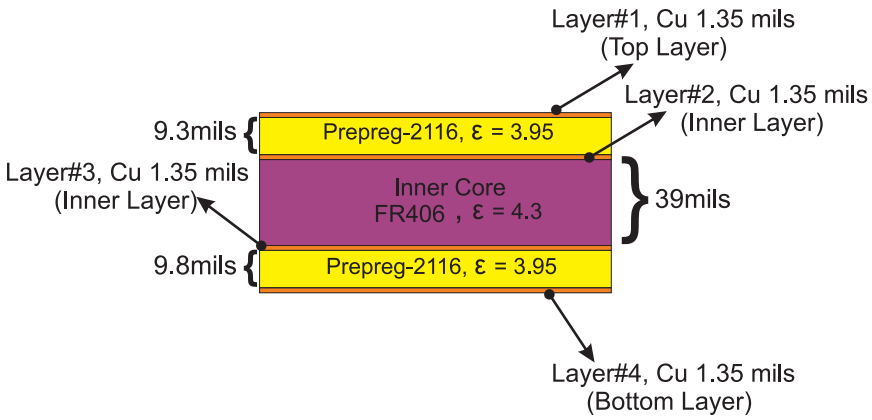

Figure 13: FR-406 4-layer stack-up used for the RF tag. An inner layer of FR-406, a high performance epoxy material is inserted between two layers of Prepreg-2116 which is resin-impregnated woven fiberglass. The top and bottom layers are used for signaling and antennas, one inner layer is used as a ground plane, and the other inner layer is unused.

dielectric constant and low dissipation factor make it an ideal candidate for circuit designs requiring better signal integrity. The prepreg–2116 has a relative permittivity $\epsilon_r = 3.95$ with loss tangent $\sigma = 0.019$, while the inner core FR-406 has $\epsilon_r = 4.3$, with $\sigma = 0.016$ [25]. As a first step, the partitioned loop antenna was simulated without the addition of a ground plane in HFSS software, which produced an omni-directional gain pattern with the null in the z-direction, i.e., normal to the plane of the loop. The simulation results for this antenna are shown in Figure 14 and Figure 15. The resonance frequency was observed to be 5.8 GHz with an S11 of -19.8-dB. The 3-D gain pattern depicts the null in the z-direction. The pattern in all principal planes are also given, depicting the symmetrical coverage in Y–Z and X–Z planes. The X–Y plane, which is also the plane of the PCB, depicts omni-directional coverage with slight dips. The antenna was horizontally polarized, i.e, X–Y is the plane of polarization.

In order to integrate the antenna with rest of the RF-tag circuit, a ground plane was added and then re-simulated in HFSS. As stated earlier, the antenna was directly integrated with the RF switch at its feed. For this purpose, the ground pad of the

RF switch with vias was also simulated with the final antenna design. Figure 16 shows the layout of the antenna with overlapping portions highlighted. The large portion in the bottom of the figure represents the ground plane. Figure 17 and Figure 18 illustrate the antenna radiation patterns in the X–Y, Y–Z, and X–Z planes whose omni-directional characteristics have been distorted by the presence of the ground plane and tag electronics. Simulations further showed the maximum resonant frequency of the antenna to be 5.77 GHz with an impedance of $49.87 - 0.08j\ \Omega$, S11 of -56.5 dB and a 10 dB bandwidth of 600 MHz. By further optimization of the overlapping patches and adjustments to the ground plane, a more omni-directional pattern could be realized.

3.3.1 Design of Two Partitioned Loop Antennas

The top two layers of four-layer FR-406 substrate material were used for the case of a single antenna. A replica of the same antenna was placed on the bottom two layers by rotating it by 180° in the opposite direction. The antennas were placed one free-space wavelength apart to avoid coupling and are equidistant from the microcontroller. Figure 19 shows the orientation of the antennas and the tag itself with respect to the reader, where R is the distance from the tag to the reader, d is the distance between the antennas, α is the random orientation of the tag with the respect to reader and E_1 and E_2 are backscattered E-fields from the two antennas. Each antenna was excited with its own independent constant power excitation source in HFSS. This design is different from a phased-array configuration because the RF received at the antennas is never combined. In effect, these are two different antennas modulating a coherent incident wave in parallel. Figure 20 and Figure 21 illustrate the antenna radiation patterns in the X–Y, Y–Z, and X–Z planes whose omni-directional characteristics have been distorted by the presence of the ground plane and tag electronics. The maximum resonant frequency of both the antennas was approximately 5.79 GHz with

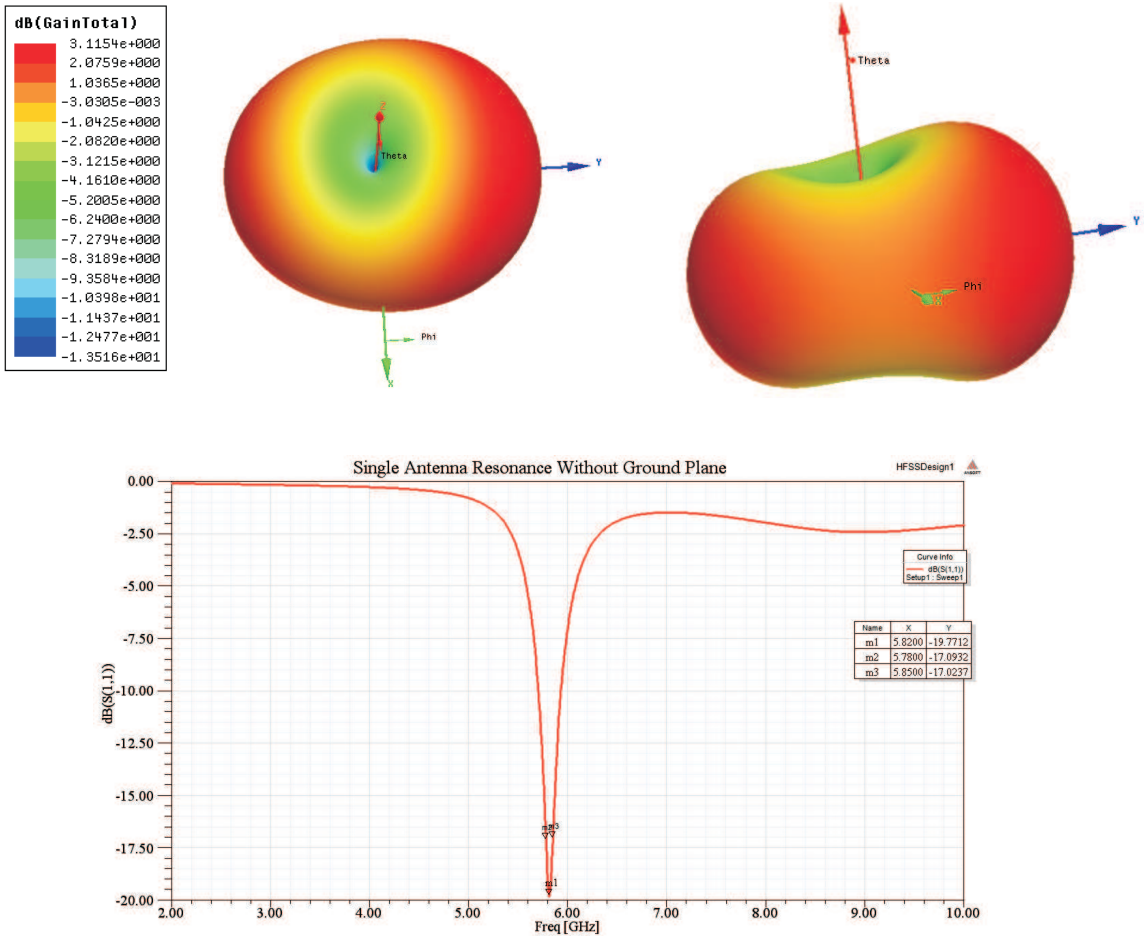

Figure 14: Simulated HFSS radiation pattern of the partitioned square-loop antenna in the X–Y, Y–Z, and X–Z planes without ground plane with omni-directional gain pattern. Maximum resonance was observed at 5.8 GHz with an S11 of approximately -20 dB.

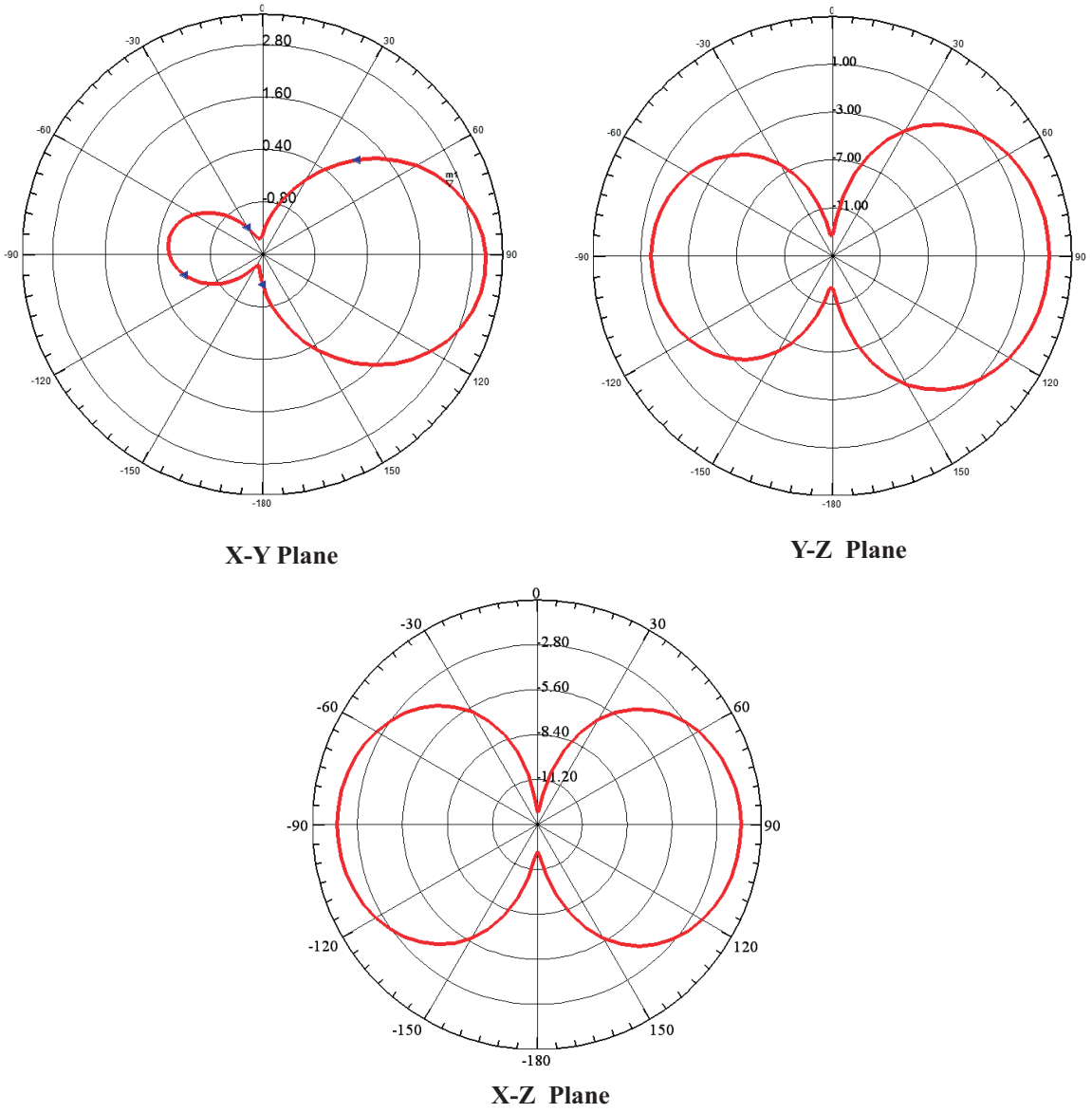

Figure 15: Simulated HFSS radiation pattern of the partitioned, square-loop antenna in the X–Y, Y–Z, and X–Z planes without a ground plane. These patterns depict an omni-directional gain pattern.

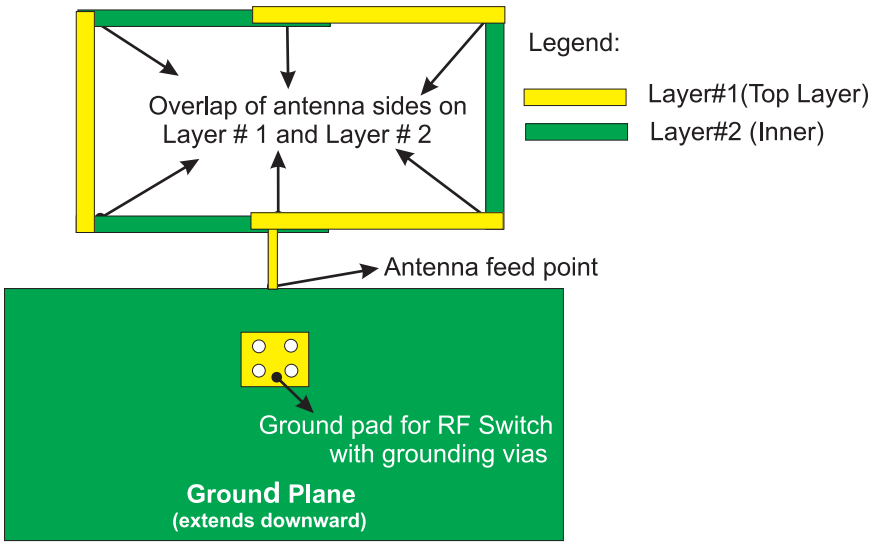

Figure 16: Partitioned, square-loop antenna layout. Alternating sections of the antenna occupy different layers of the PCB which capacitively loads the antenna in order to reduce phase variation across the antenna sides.

an impedance of $53 + 4j\ \Omega$, S11 of -26.5-dB and a 10-dB bandwidth of 600 MHz. It is worth mentioning here that the simulated impedance is required for the transmission where as in this work the antennas practically do not transmit any signal. They instead backscatter the incident RF waves.

3.4 Range and Radar Cross-section Improvement using Multiple Antennas

Several antenna techniques have been suggested in order to improve the radar cross-section (RCS), range and reliability of RFID tags including phased array antennas on the reader [26], multiple tag antennas to improve the power available for energy conversion [27], and multiple tag antennas to reduce tag orientation sensitivity [28] among others. Griffin discusses the benefits of multiple reader and tag antennas in [29] to improve the resilience against small scale fading in backscatter radio systems. Using multiple antennas at UHF frequencies may not be desirable because of the size of the footprint associated with antennas at this frequency. However, 5.8 GHz antennas are

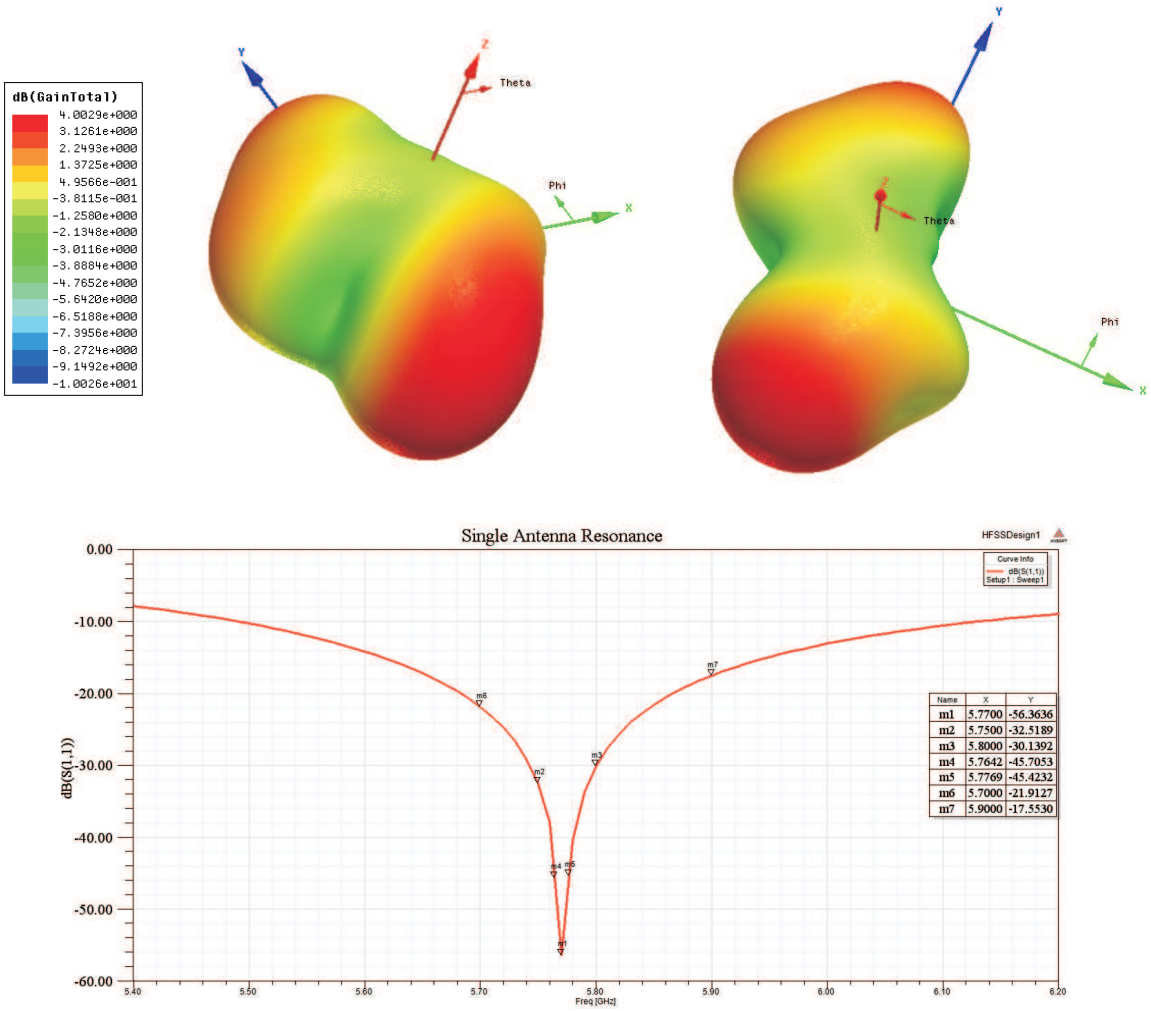

Figure 17: Simulated HFSS radiation pattern of the partitioned, square-loop antenna in the X–Y, Y–Z, and X–Z planes whose omni-directional characteristics have been distorted due to the presence of the tag's ground plane. Maximum resonance was observed at 5.77 GHz with an S11 of -56.5 dB.

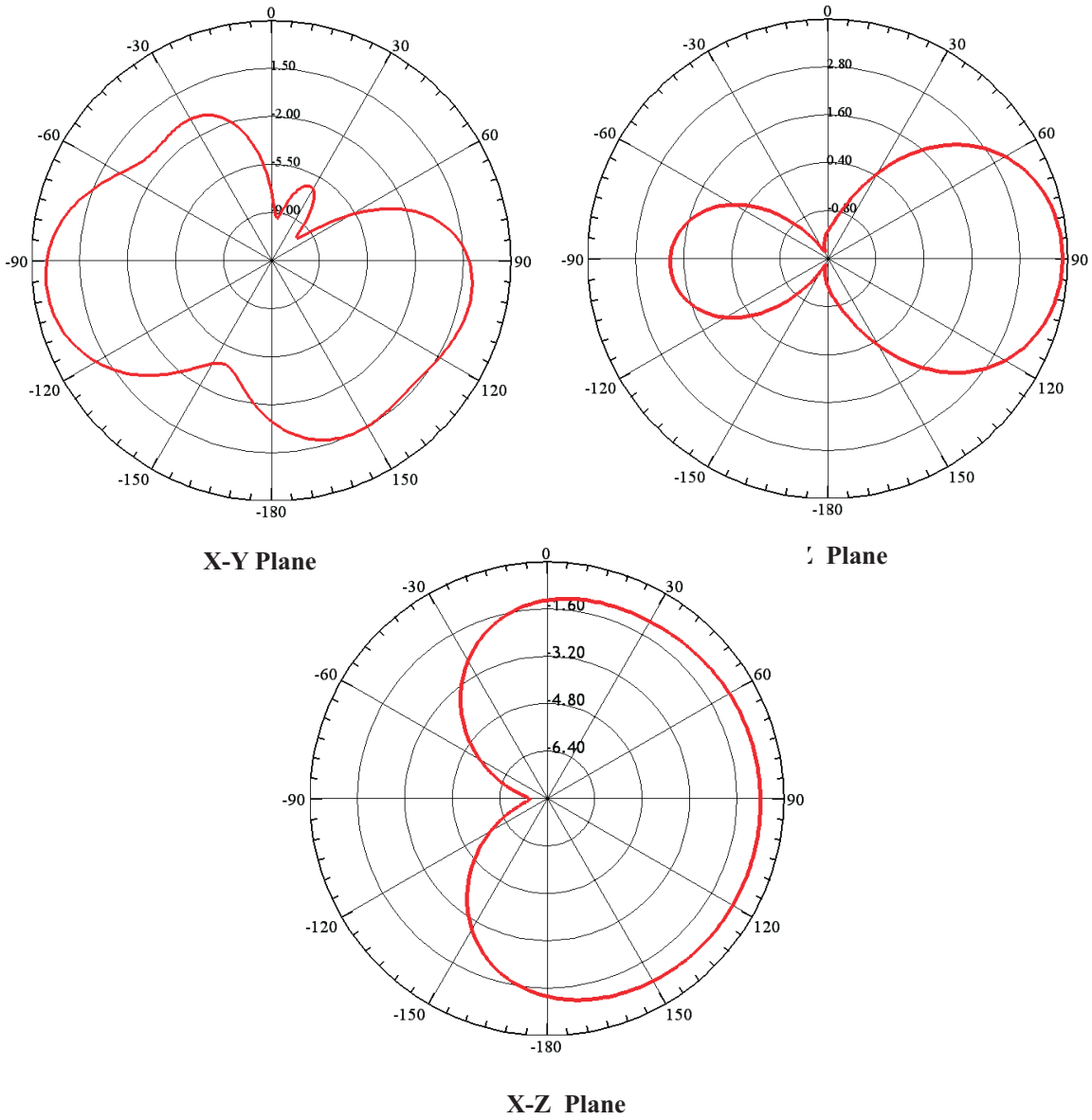

Figure 18: Simulated HFSS radiation pattern of the partitioned, square-loop antenna in the X–Y, Y–Z, and X–Z planes whose omni-directional characteristics have been distorted by the presence of the tag's ground plane.

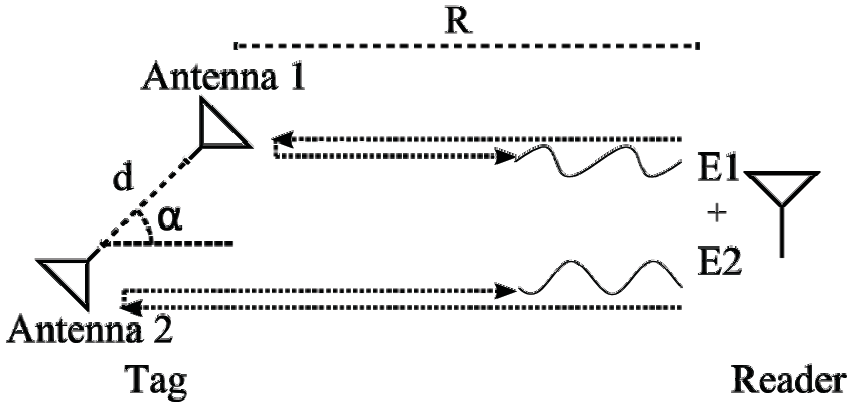

Figure 19: Both the antennas are oriented 180° in the opposite directions, where R is the distance of the tag from the reader, d is the distance between the antennas, α is the random orientation of the tag with the respect to reader, and E_1 and E_2 are backscattered E-fields from the two antennas.

nearly 15% the size of an antenna at 900 MHz. Thus, multiple antennas at 5.8 GHz can fit within the same footprint as a UHF tag with a single antenna. This section compares the range performance of two tags (single and dual antenna configurations) based on the improvement in RCS due to multiple antennas. Theoretical analysis, simulated and measured results are discussed in subsequent paragraphs. Most of the work in this section has been adapted from [1].

3.4.1 Theory and Simulations

Increasing the number of antennas on the tag increases its radar cross section. Therefore more power is backscattered which improves the read range. The range of a tag with N antennas can be related to a single antenna tag by [28]

$$r_N = Kr \qquad 1 \leq K \leq N, \tag{23}$$

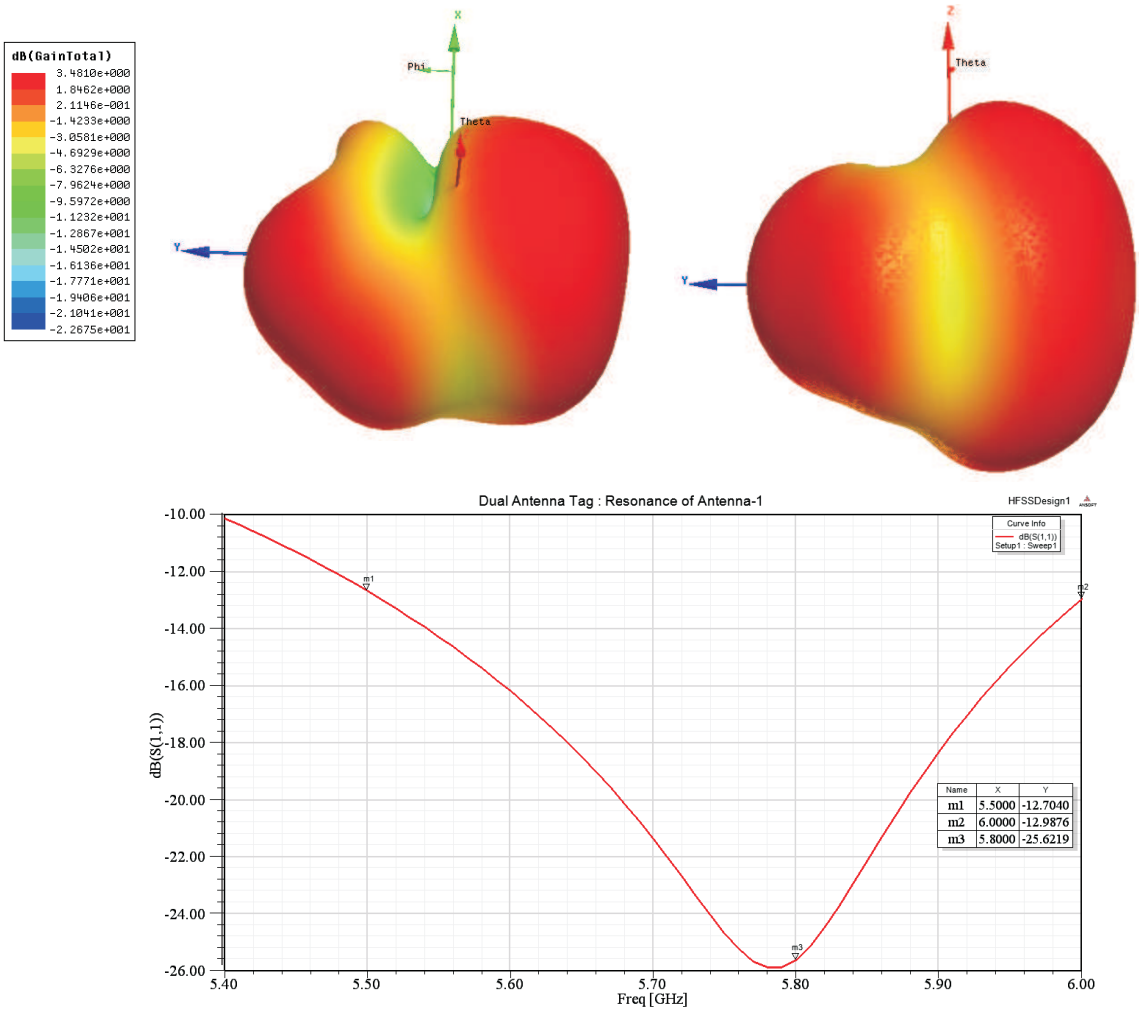

Figure 20: Simulated HFSS radiation patterns of the dual antenna tag in the X–Y, Y–Z, and X–Z planes whose omni-directional characteristics have been distorted by the presence of the ground plane and tag electronics. Overall the pattern has improved compared to a single antenna tag. Maximum resonance was observed at 5.79 GHz with an S11 of approximately -26.5 dB.

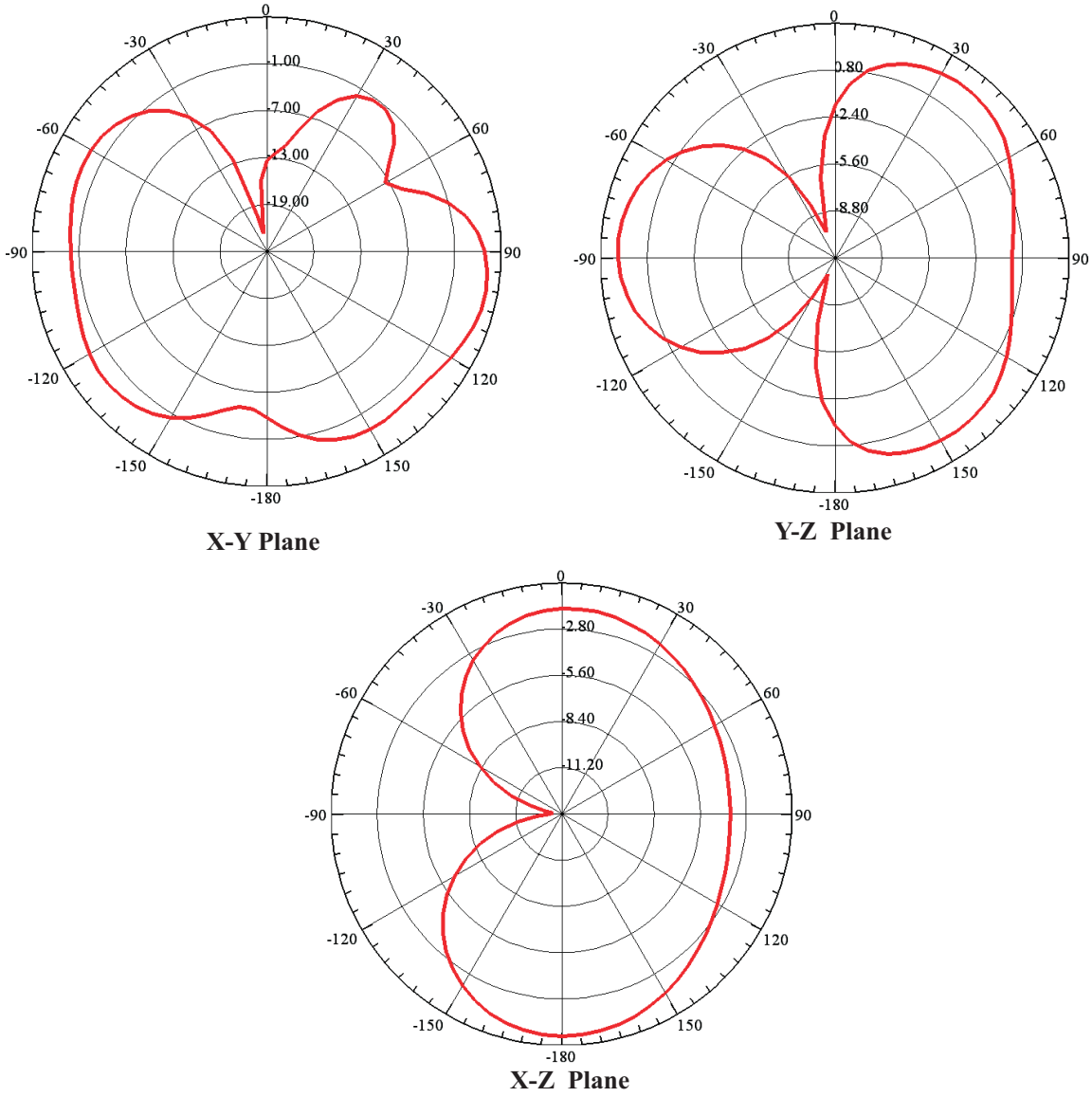

Figure 21: Simulated HFSS radiation patterns of the dual antenna tag in the X–Y, Y–Z, and X–Z planes whose omni-directional characteristics have been distorted by the presence of the ground plane and tag electronics. Overall the pattern has improved compared to a single antenna tag.

where K is range increase factor. In free space, the maximum possible range increase would therefore be N. Moreover, multiple antennas considerably reduce the fading which corresponds to increased reliability and read range [29].

Each antenna is treated independently since there is no common load. The structure is modeled as two identical antennas, with one flipped around the x-axis by 180°, making the two directly opposed to each other as given in Figure 19 and Figure 8 of Chapter 2. The simulated gain of antennas in High Frequency Structure Simulator (HFSS) software is used to find the backscattered power density at the reader according the the bi-static co-located link budget [5]. The power density at the reader is translated into an electric field magnitude, and then normalized by the electric field polarization components as simulated in HFSS, incorporating both magnitude and phase. The phase offset of the backscattered signal due to the tag antennas' separation and orientation is incorporated into one of the antenna's electric field, and the two fields are summed and converted back to a power. The sum is added back into the link budget given in [5] to find the portion that represents the radar cross section (RCS) given in equation (24) that is generalized for N antennas from [5]. In equation (24), σ_{RCS} is radar cross section, λ is the wavelength, N is the number of the antennas, $G_n(\theta, \phi)$ is the simulated gain and $\vec{E_n}$ is the simulated electric field vector phasor component of the n^{th} antenna. The RCS is normalized by the antenna-load reflection coefficient $|\Gamma|$ for generality, and this RCS does not include the un-modulated structural RCS. In this work, we are dealing with a special case, where $N = 2$ (i.e. two antennas), $\phi_1 = 0$, $\phi_2 = \frac{4\pi}{\lambda} d \cos\phi$ and d is the distance between two antennas in X–Y plane.

$$\frac{\sigma_{RCS}}{|\Gamma|^2} = \frac{\lambda^2}{4\pi} \left\| \sum_{n=1}^{N} G_n \hat{e}_n \exp(j\phi_n) \right\|^2 \qquad where \quad \hat{e}_n = \frac{\vec{E_n}}{\left\| \vec{E_n} \right\|} \tag{24}$$

The RCS normalized by the antenna load reflection coefficient is calculated and plotted on linear scale in MatLab and shown in Figure 22. It can be seen that the RCS

for multiple antennas is larger than that of a single antenna. The presence of nulls in the dual antenna RCS stems from the destructive interference of the two backscattered signals. The antennas were designed to receive / backscatter, horizontally polarized signal in PCB plane (i.e. X–Y plane).

3.5 Experimental Setup to Measure RCS and Results

The tags were mounted on a rotary platform, with a random set of data repeating at a 2.5 MHz bit rate, approximately 1 meter away from a bi-static reader. Raw, demodulated IQ data was taken for 360° in all principle planes to assess the tags' RCS at 5.8 GHz. Polar plots of the normalized linear magnitude of this data was plotted using MatLab and is given in Figures 23 and 24. The reader's signal was horizontally polarized, which matches the tags' polarization in the X–Y plane only. Therefore all principle planes were mounted on rotary form in such a way that no polarization mismatch occurs in other planes. The recorded RCS of both the tags was also plotted using MatLab by overlapping the data from both the tags and normalizing it by the maximum value from dual antenna tag. Figure 25 shows that the differential RCS of the dual antenna tag is 1.8 times larger than that of a single antenna tag in the plane of polarization. Similar experiments were conducted for read range assessment for both the tags by finding the distance over which the tags backscattered signal can be successfully demodulated. It was observed that the read range with the dual antenna tag is 1.3 times larger than that of single antenna tag. The tag data is displayed in two portions on a graphical user interface (GUI). One portion is for the shock in *g-values* on all three axis and the other is for resultant rotation due to impact in *degrees per sec* on all three axis. A screen shot of the *GUI* is given Figure 26, where all the high peaks show the impact experienced by the tagged object.

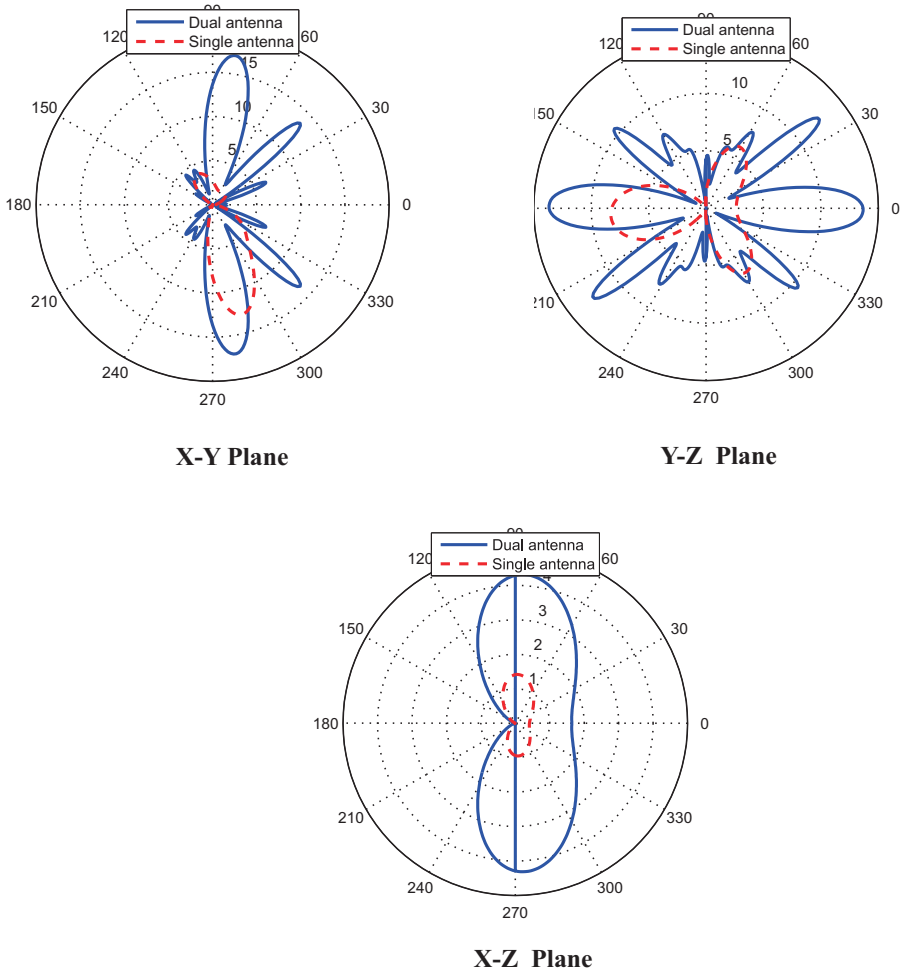

Figure 22: Radar cross sections in cm^2 normalized by reflection co-efficient [Γ] for X–Y, Y–Z and X–Z planes of the tag for ϕ–polarized incident wave. (Reprinted from [1] © 2012 IEEE)

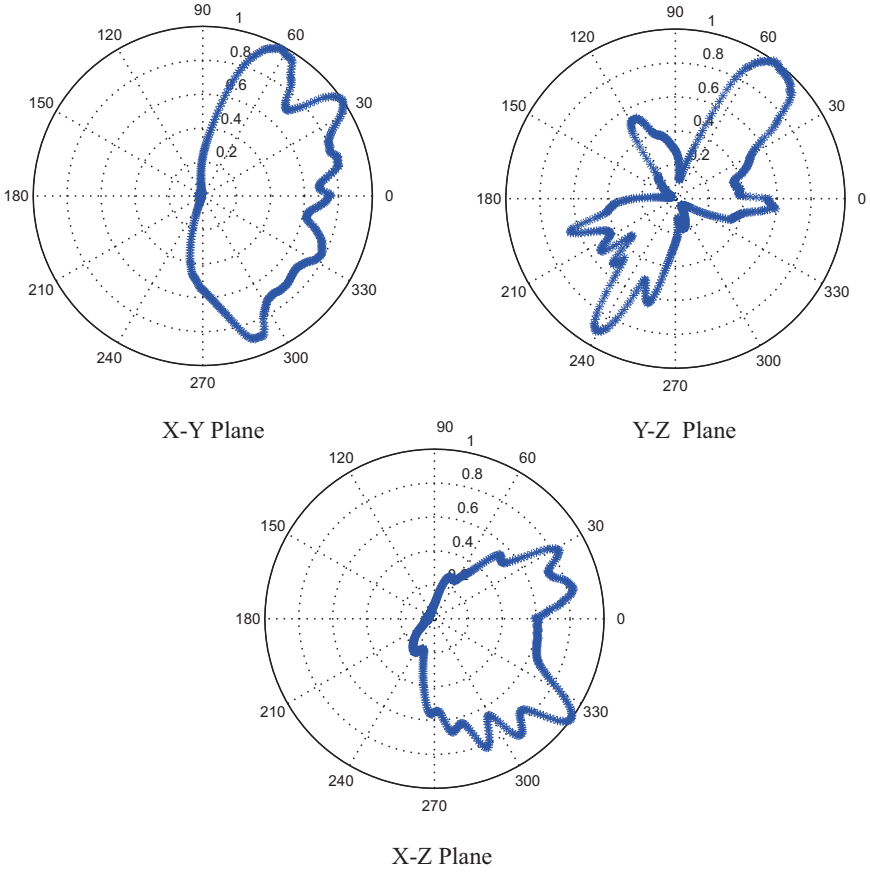

Figure 23: Measured RCS of a single antenna tag. The RCS differs from the radiation pattern because the tag is battery operated with electronics installed that shift the RCS pattern in the plane of polarization, i.e., X–Y plane.

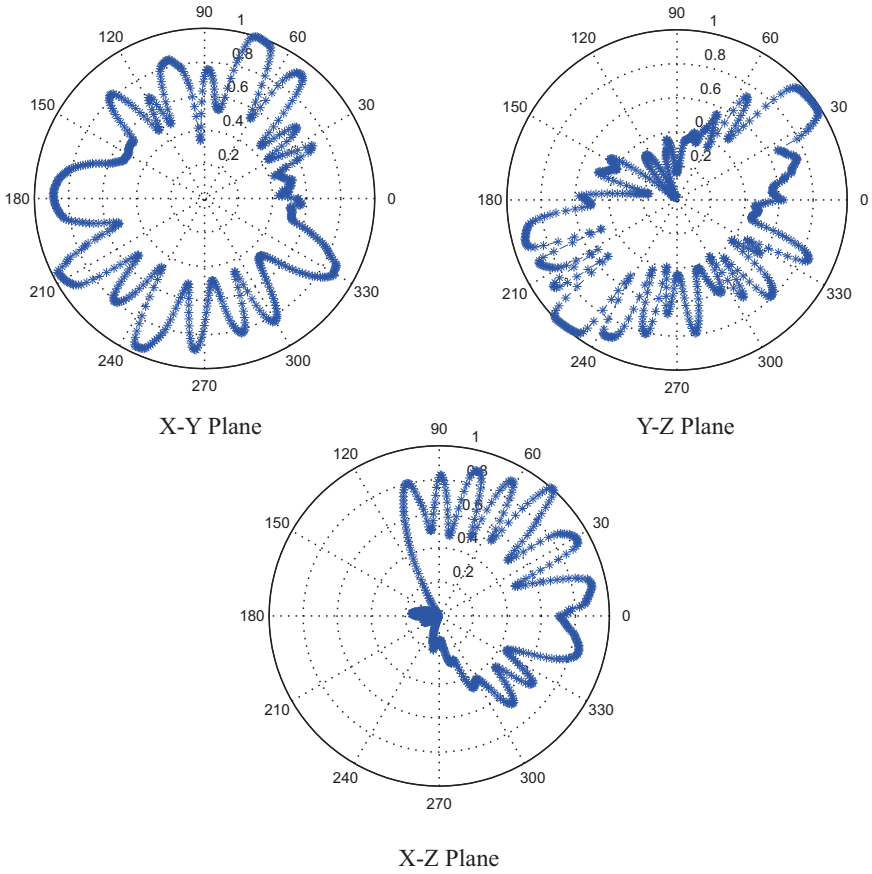

Figure 24: Measured RCS of dual antenna tag.Overall RCS improves in all directions due to presence of antenna at both ends of the tag.

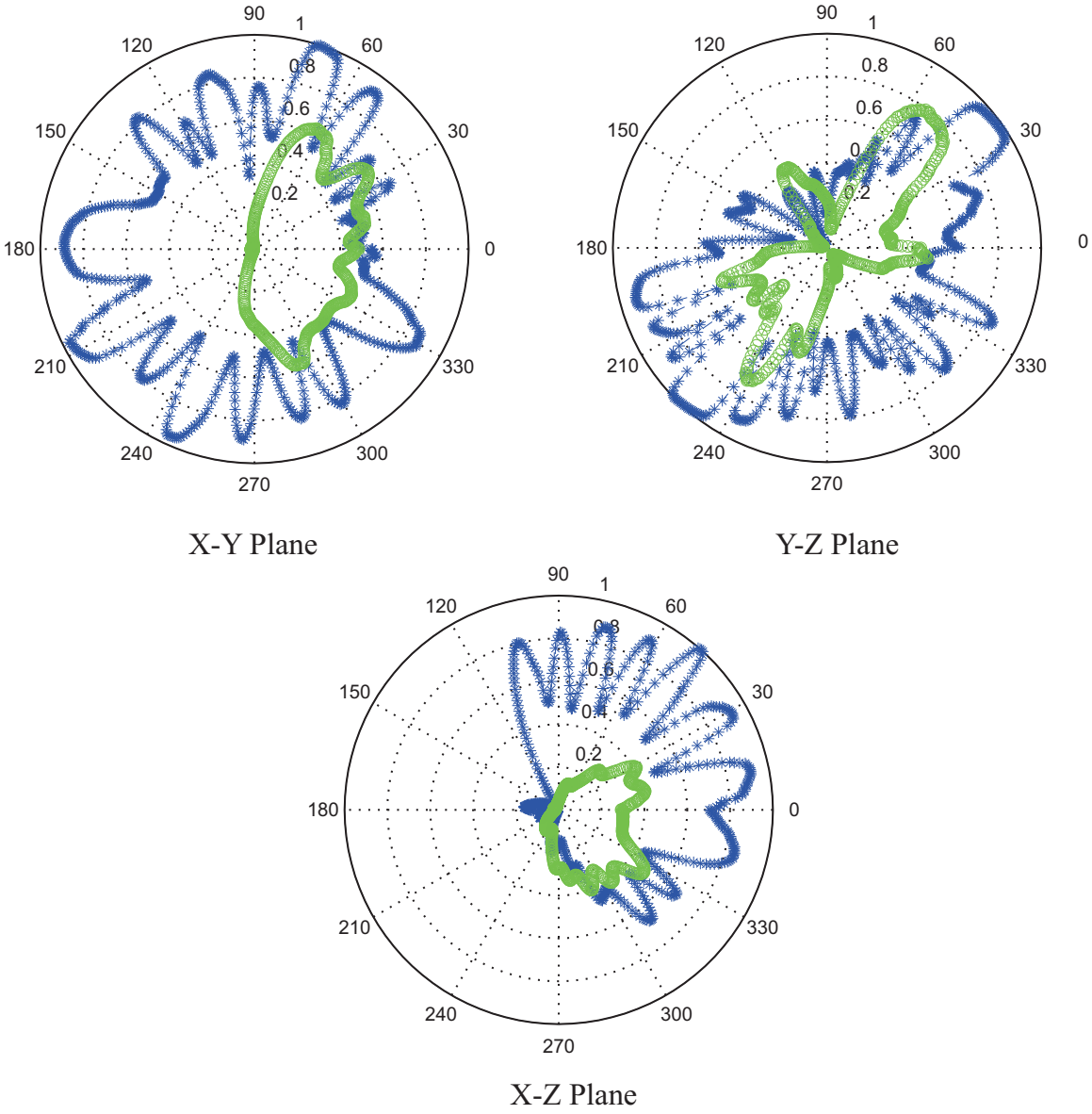

Figure 25: Overlapped measured RCS of single and dual antenna RF tags in the plane of polarization. The measured RCS of the dual antenna tag is 1.8 times larger than the single antenna tag.

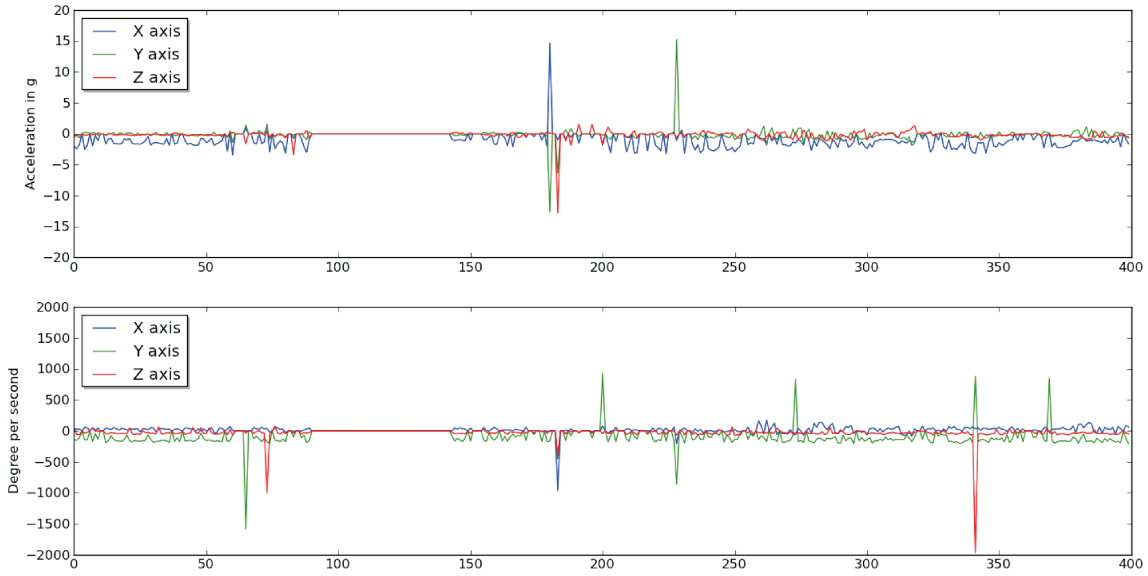

Figure 26: A screen shot of the *GUI*. The upper half shows the shock/impact in g-values experienced by the tagged object showing peaks at shock/impact instants. Corresponding peaks in the lower half show the angular motion in *degrees per sec* of the tagged object due to impact. All the axis are color coded for clarity.

3.5.1 Conclusion

Multiple antennas can help increase the read range of the RF tags and at higher frequencies such as 5.8 GHz, the antennas' size is small so the overall footprint of the tag stays within reasonable limits. Moreover, the tag with dual antennas has increased RCS, which plays a major role in range improvement. An improvement in the range by a factor of 1.3 was observed with dual antennas as compared to a single antenna.

CHAPTER IV

FUTURE WORK

4.1 Introduction

Since the inception of the backscatter transponder concept, much effort has been put in to research in the area of RF tag technology development [30]. Available RF tag environments can be exploited in various ways (like access control, electronic tolling, asset management etc). An extremely important application is localization of the RFID tag.

The value of RFID technology is greatly diminished if one cannot locate an RF tag [31]. Traditional positional approaches based on Received Signal Strength Indicator (RSSI),Time difference of Arrival (TDOA), Angle of Arrival (AoA), Return Time of Flight (RTOF) and other wireless local positioning schemes are all applicable to determine the position of the RF tags [32]. Position locating can also be done using the Frequency Modulated Continuous Wave (FMCW) radar principle in backscatter RFIDs [33]. But each technique has inherent limitations such as complexity, lack of accuracy, and high cost. In the majority of applications these approaches use one type of measured information to locate and track.

Besides the positioning techniques discussed in [32], the phase information of the backscattered signal in RFID can also be manipulated to extract the position and velocity of the tagged object. The phase information is important because RFID readers use the same clock (oscillator) for transmission and backscattered reception. Therefore, the receivers carry-out synchronized signal detection and coherent demodulation of the received signal to retrieve tag information. This is not generally the case for conventional wireless communication where separate unsynchronized clocks

(oscillators) are used in transmitters and receivers. William, *et. al* [34] utilize phase information from an RFID tag for positioning but used an incoherent active tag that transmits at 433.92 MHz. The phase information is extracted using two coherent software-defined radio receivers. Nikitin, *et. al* [35] illustrates three phase difference of arrival techniques in the time, frequency and spatial domain, respectively, and experimentally demonstrates a time domain based phased difference of arrival technique using Gen2 tags with a customized reader. Miesen, *et. al* [31] describes a holographic positioning scheme based on sampled phase values along a trajectory of a UHF RFID tag.

Solid state accelerometer and gyroscopes have consistently been used for platform stabilization in control systems [36], image stabilization in cameras and handsets [37], human body motion tracking, gesture and posture tracking [38, 39, 40], test vehicle tracking [41] and robot navigation, pedestrian navigation systems [42, 43] and many other applications [44]. Most of the references cited above either installed the MEMS (accelerometer, gyroscopes, etc) on the object of the interest and used commercially-off-the-shelf available 433.92 MHz and 2.45 GHZ ISM band radios to transmit the data back to the receiver for processing of human body motion or gesture tracking. Jackson and Callahan, [41] used MEMS for tracking the location of an object in an indoor scenario.

This chapter discusses the localization technique of backscatter RF tags using the combination of the phase difference and inertial sensor (accelerometer) data, using a technique called Hybrid Inertial Microwave Reflectometry (HIMR).The accelerometer data is backscattered by the RF tag on digital data packets. Section 4.2 describes in detail the proposed localization technique. Section 4.3 outlines the implementation of the proposed technique.

4.2 Proposed HIMR Scheme for Localization

HIMR allows a degree of tracking which is not possible with just inertial and phase-based measurements. It allows more accuracy and adds reliability to tag tracking by providing information that can be manipulated in various ways to get the instant location. In this scheme the tag under consideration senses the acceleration of the object on which it is installed and backscatters the sensed acceleration to the reader. The tag can be tracked by measuring the phase shift and demodulating the sensed backscattered acceleration at the reader. For simplicity two dimensional movement is considered which can later be generalized for three dimensions. The case under consideration is shown in Figure 27. In 2-D, the sensed acceleration consists of two components and can be written as

$$\vec{a} = \vec{a_x} + \vec{a_y} \tag{25}$$

where $\vec{a}$ is the total acceleration vector, $\vec{a_x}$ is the acceleration vector along the x-axis and $\vec{a_y}$ is the acceleration vector along the y-axis.

Co-located transmitter and receiver antennas are assumed to be static and located at the origin (x_o,y_o) of the system. To further simplify the scenario it is assumed that the initial position and distance (ρ_o, Φ_o) of the tag with respect to the origin is known. The tag is oriented at an angle of α with respect to original (x,y) axis and is moving towards the origin. Before going into further details, let us explain the concept of phase shift in the system under consideration.

To illustrate the concept of phase shifts, first consider the case of a static transmitter transmitting digitally encoded symbols to a static receiver. In conventional wireless radio systems, the transmitter has an oscillator that generates the carrier and modulates the coded symbols. These coded symbols follow a constellation diagram that depends upon the modulation scheme used to transmit the symbols. There is an unknown length of distance that the radio signal has to traverse in order to reach the

receiver. In doing so, the signal undergoes an unpredictable amount of phase change. Every distance it accumulates adds phase offset to the transmitted signal that moves the constellation diagram. In a general wireless system the receiver does not have the exact copy of the transmitter's oscillator. Although the frequency source (the local oscillator) in the receiver can be in agreement to the ten-millionth part with a transmitter oscillator, this still leaves a sizable offset of hundreds or thousands of Hertz. This affects the in–phase and quadrature–phase channel measurements. If the transmit and receive frequencies are not perfectly synchronized, it will add a slow rotation to the in–phase and quadrature–phase channel measurements. So even if somehow the phase difference between the transmitter and the receiver is known exactly, and decision boundaries are marked, the signal constellation continues to gyrate sporadically, with no meaningful phase reference.

As mentioned earlier, in case of RF backscatter systems, the transmitter and receiver are perfectly coherent because they share the same local oscillator. Thus, there is no phase difference due to the oscillator, and the constellation will stay perfectly stable. Now the constellation will only rotate if the RF tag moves in any direction depicting the phase shift due to motion. Considering that RF tag sends different data each time it backscatters, the phase shift due to motion can now be observed in each received packet. By different data it is meant that each packet has new acceleration information and hence a new combination of symbols. Since the packets are periodic and have new data each time, the phase shift can be measured by comparing the phase of the symbols in preamble/header data in each packet with respect to previous packet. The header symbols are the same in every packet and would be a good reference for phase shift calculation.

In any propagation environment, the phase of the received signal can be written as [35]

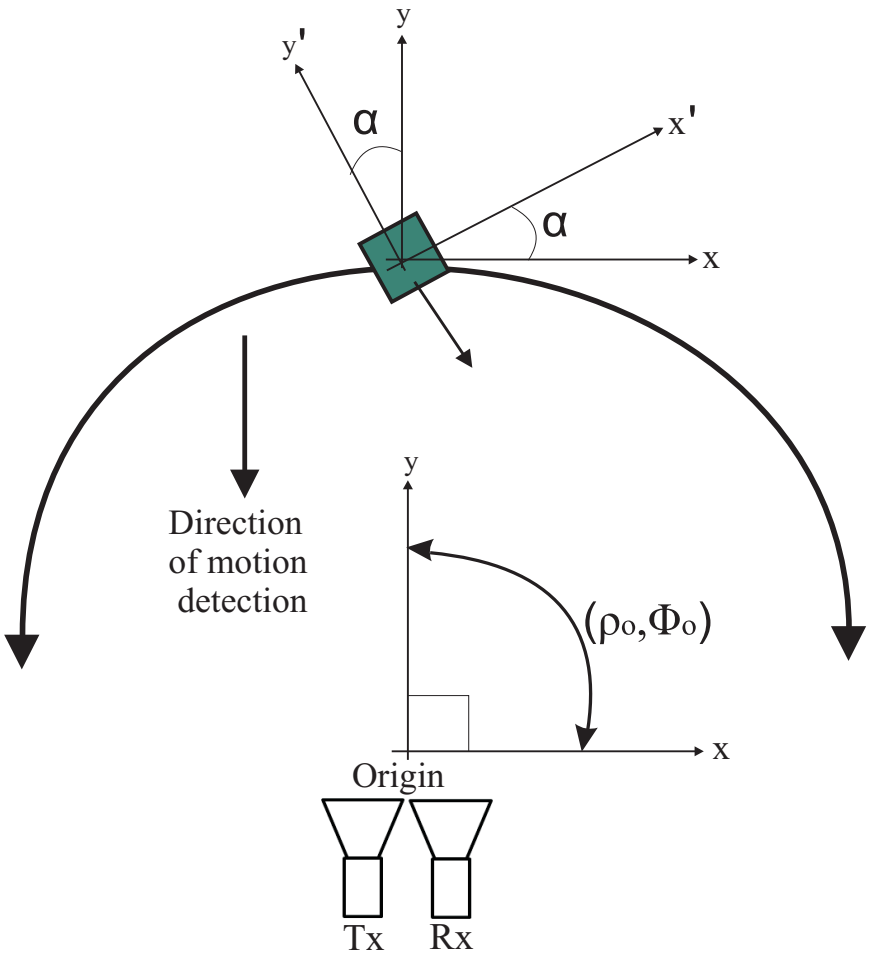

Figure 27: Two dimensional depiction of localization geometry using the proposed HIMR technique. Static and co-located transmitter and receiver antennas are located at the origin (x_o,y_o). The tag is oriented at an angle of α with respect to the original (x,y) axis and is moving towards the origin.

$$\phi = \phi_{prop} + \phi_o + \phi_{BS} \tag{26}$$

where ϕ_{prop} is the phase accumulated due to the electromagnetic wave propagation, ϕ_o is the phase offset which includes phases of the cables and other reader and antenna components, and ϕ_{BS} is the backscattered phase of the tag modulation.

By measuring the phase of the tag signal at two different time instants (at fixed frequency), assuming that the other two components of the tag phase do not change,

and taking the derivative of the phase with respect to time, we can calculate the tag radial velocity vector $\vec{V_r}$ as

$$\hat{\rho} \cdot \vec{V_r} = \frac{1}{2k} \frac{\partial \phi}{\partial t} \tag{27}$$

In Cartesian co-ordinates we can write the above equation as (refer to Figure 27)

$$\begin{bmatrix} \cos(\Phi_o) & \sin(\Phi_o) \end{bmatrix} \begin{bmatrix} V_x \\ V_y \end{bmatrix} = \frac{\lambda}{4\pi} \frac{\partial \phi}{\partial t} \tag{28}$$

where Φ_o is the bearing angle of the tag with respect to origin, ϕ is the phase of the received signal and k is the wavenumber. Assuming no bias error in the accelerometer data $\vec{a}$, we can express the radial velocity vector $\vec{V_r}$ as the integration of acceleration vector $\vec{a}$.

$$\vec{V_r} = \int_0^t \vec{a} dt \tag{29}$$

In terms of the tag orientation angle α with respect to the original x, y–axis, (see Figure 27) the above equation 29 can be written as

$$\begin{bmatrix} \cos(\alpha) & -\sin(\alpha) \\ \sin(\alpha) & \cos(\alpha) \end{bmatrix} \begin{bmatrix} V_x \\ V_y \end{bmatrix} = \left\| \int_0^t \vec{a} dt \right\| \tag{30}$$

In equations (28) and (30), the acceleration, $\vec{a}$, measured by the accelerometer, the bearing angle, Φ_o, and the phase of the packet measured by the backscatter receiver, ϕ, are the known quantities, whereas tag orientation angle α, and velocity components V_x and V_y are unknowns. Equation (30) is actually a matrix representation of two equations. These three equations can be simultaneously solved to find the unknown quantities. After simultaneous solution, the tag orientation angle α comes out to be

$$\alpha = \theta_o - \Phi_o + \arccos\left(\frac{P}{\left\|\int_0^t \vec{a}dt\right\|}\right) \tag{31}$$

where

$$P = \frac{\lambda}{4\pi}\frac{\partial\phi}{\partial t} \tag{32}$$

and

$$\theta_o = \arctan\left(\frac{a_y}{a_x}\right) \tag{33}$$

The acceleration values a_x and a_y of the tag can be used in equations of the motion to determine the distance 'd' it traveled in the time interval between each packet. Direction of motion can easily be determined from the sign of acceleration data values, a_x and a_y, sent by the tag. This produces

$$d_x = V_{ix}t + \frac{1}{2}a_x t^2 \tag{34}$$

where d_x is the distance along the x-direction and V_{ix} is the initial velocity along the x-axis.

4.3 Implementation of the Proposed Scheme

A portion of baseband data from a custom developed RF tag for 5.8GHz is shown in Figure 28. The same digital data is being transmitted on both I and Q-channels.

Each bar represents a single data packet consisting of preamble / header, RF tag ID and sensed acceleration data. The data is modulated using differential binary shift keying (DBPSK). The modulated packet at the baseband looks like Figure 29.

The start of preamble / header in the entire data stream can be located by the circular-cross-correlation of a raised cosine sync-sequence depicted in Figure 30 with the baseband tag data. After identifying the start of the packet header, the phase

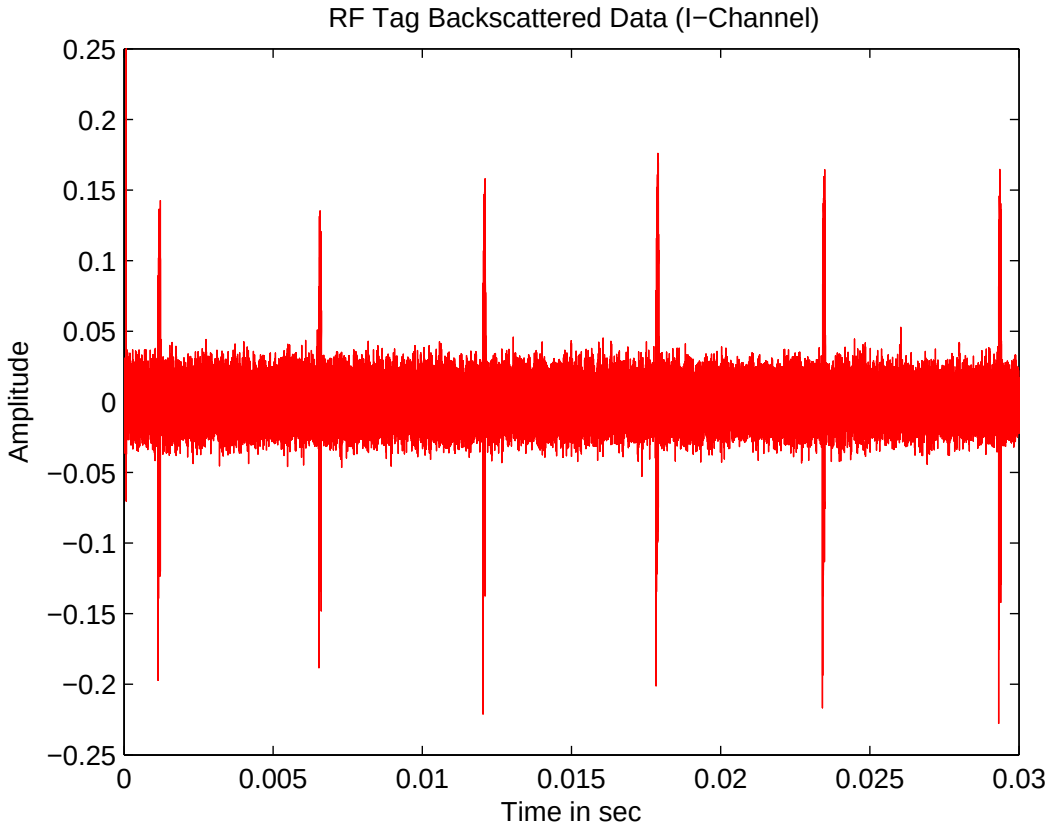

Figure 28: A portion of the baseband data from RF tag.

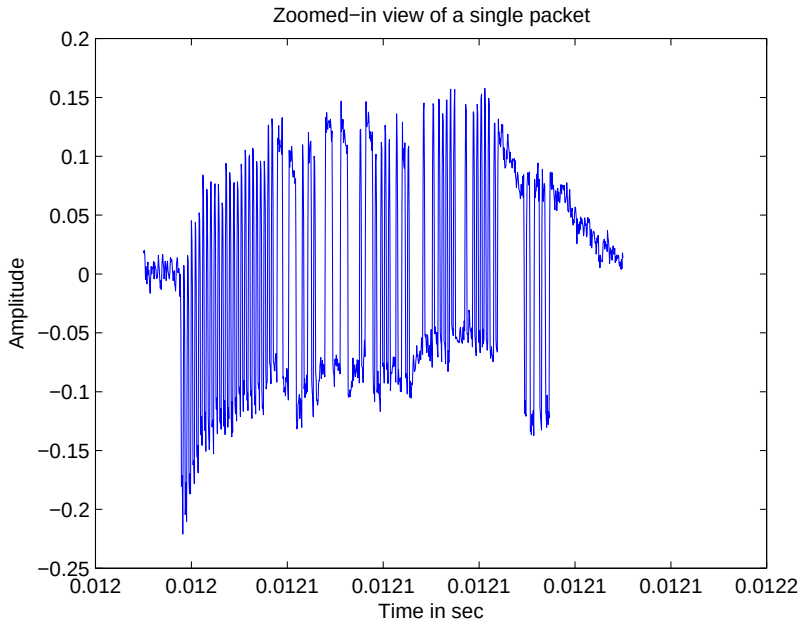

Figure 29: Zoomed-in view of a single backscattered packet from RF tag.

of each packet header can be calculated individually in the receiver by using I-Q-channel data. The phase of each preamble has some mean μ_ϕ and variance σ_ϕ^2. This can be used to find phase differences from packet to packet. One such attempt where the phase of three consecutive packets randomly selected from the data stream using MatLab is illustrated in Figure 31.

The demodulated acceleration data along with the measured phase difference can be used in the proposed scheme explained in detail in section 4.2 to find the velocity, the direction of motion and the distance traveled by the tag, hence implementing RF tag tracking using the Hybrid Inertial Microwave Reflectometry technique. A robust algorithm is needed to be developed which can take the baseband signal data from the receiver and perform the calculations as per the proposed scheme. With more experiments the HIMR scheme can be evolved to make it strong, error free and useful. The author is currently working on the viability and validity of the HIMR scheme. If succeessful the proposed scheme can be extended to higher dimensions with inclusions

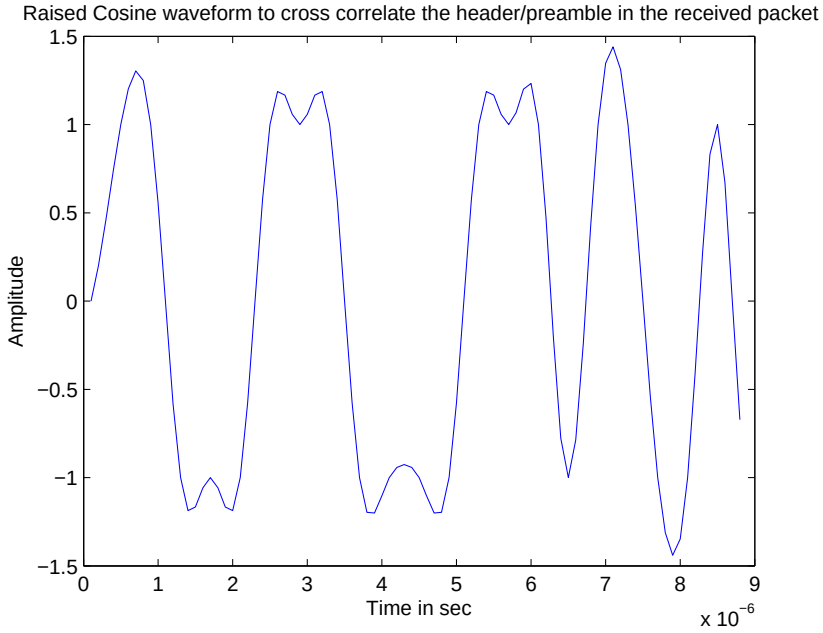

Figure 30: Raised cosine waveform generated in Matlab to cross-correlate it with the received packet to find the start of the header in the baseband data stream. A root raised cosine waveform is used because it matches the received packet waveform. Once the start of the header in each packet is found after cross correlation, then the change in phase from packet to packet can be calculated easily.

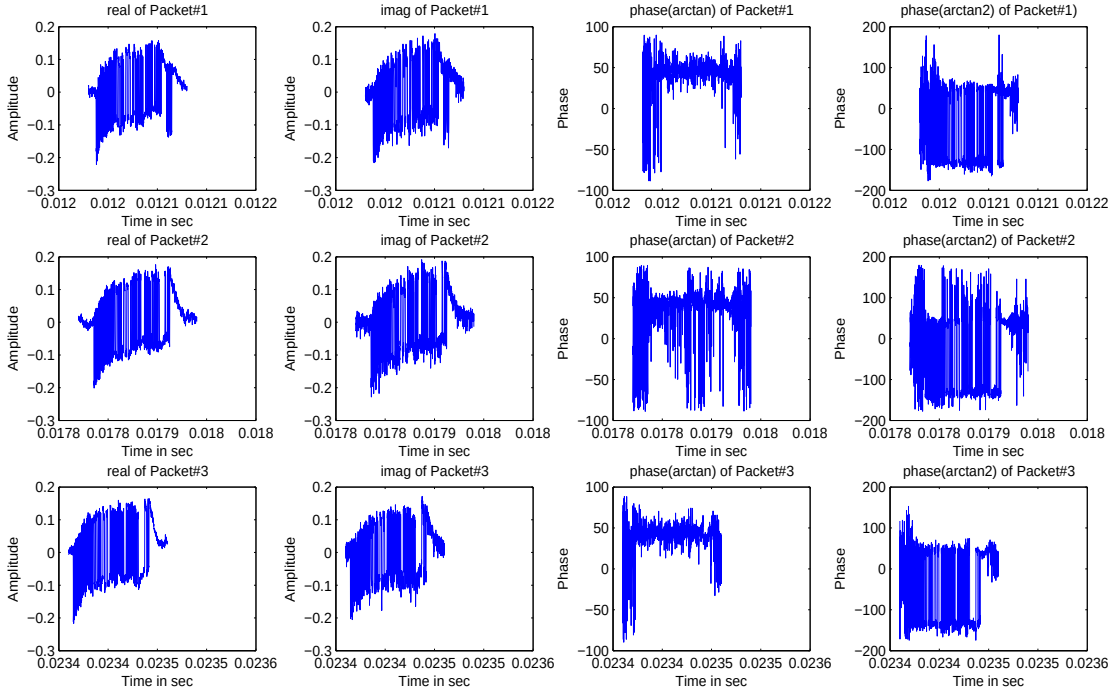

Figure 31: Three randomly selected consecutive data packets to illustrate the phase changes. Packet to packet phase change can be observed in last column of the above figure.

of many more variables such as the effect of gravity, tracking the tag without knowing the initial position or assuming tighter assumptions.

4.4 Conclusion

The proposed HIMR scheme seems logical and effective in tracking the RF tag with pin–point accuracy. The initial algorithm has been proposed. Some simulation based on the algorithm has been conducted with future measurement trials in preparation. The validity of the technique can be tested using the existing 5.8 GHz transceiver and custom designed acceleration sensing tags. Rigorous testing and continuous improvement shall be required before proposing it for any application. However, when implemented it will not only broaden the localization approaches and but will also open many new avenues for tracking applications.

CHAPTER V

CONCLUSION

Overtime the head injuries and concussion to players has become a constant feature of the physical games involving player to player physical contacts like ice hockey, soccer, American football, etc. The number of such injuries has increased and lead to severe health issues for players. As such no mechanism is in place for instant monitoring of the impacts, and shocks to the head experienced by the players. This work presented a unique solution to this in form of an application of the RFID tags with the combination of MEMS based inertial sensors to instantly *detect, measure and backscatter* the *motion, shock and spin* of the tagged object.

The design involved challenges like low power consumption, planar antennas with omni-directional coverage in the plane of the tag, a higher data packet rate such that no activity is missed, and an effective data encoding scheme to achieve a system range of approximately 20 meters. For this purpose a low-power microcontroller, digital accelerometer and gyroscope were used together with a segmented square loop antenna integrated with the tag electronics through an RF switch. The microcontroller controlled all the peripherals and backscattered the sensed information by toggling the RF switch between open and short circuit loads thus implementing the two state modulation scheme. The sensed data was encoded using a Manchester encoding scheme which ensures that each bit of the data is D.C. balanced. Another advantage of Manchester encoding is that it provides a transition in the middle of the bit duration that helps in adjusting the receiver's clock. A custom data packet and protocol was designed and named the Georgia Tech Motion Protocol (GTM 1.0).

The antenna was designed on a four layer FR406 substrate material. The tags

were designed with a single and the dual antenna configurations. The azimuthal backscatter coverage was measured and the resultant change in RCS and read range due to increase in number of antennas was experimentally measured. It was observed that the RCS increased by a factor of 1.8 and range increased by a factor of 1.3 when going from a single to a dual antenna configuration [1].

Keeping in view the unique application of the tag, the developed protocol GTM 1.0 and acquired sensors dataset can be used to track the tagged object utilizing a combination of inertial data and packet to packet phase difference. This scheme was named the Hybrid Inertial Microwave Reflectometry (HIMR) and was presented for a preliminary two dimensional case with some assumptions. This can later be extended to the three dimensional case with inclusions of more variables.

REFERENCES

[1] Muhammad B. Akbar, Marcin M. Morys, Christopher R. Valenta and Gregory D. Durgin, "Range improvement of backscatter radio systems at 5.8GHz using tags with multiple antennas," in *IEEE International Symposium on Antennas and Propagation*, July 2012.

[2] Klaus Finkenzeller, *RFID Handbook*. U.S.: John Wiley & Sons Ltd, 2010.

[3] Daniel M. Dobkin, *The RF in RFID*. U.K.: Newnes, 2008.

[4] J. D. Griffin, "High-frequency modulated backscatter communication using multiple antennas," January 2009.

[5] J. Griffin and G. Durgin, "Complete link budgets for backscatter-radio and rfid systems," *Antennas and Propagation Magazine, IEEE*, vol. 51, no. 2, pp. 11 –25, april 2009.

[6] G. D. Durgin, "The hidden benefits of backscatter radio at 5.8 GHz," in *URSI*, January 2008.

[7] J. D. Griffin and G. D. Durgin, "Gains for RF tags using multiple antennas," *IEEE Transactions on Antennas and Propagation*, vol. 56, no. 2, pp. 563–570, February 2008.

[8] www.nytimes.com, "Head injuries in football," October 2010.

[9] www.riddell.com.

[10] www.cbn.com, "Helmet device could help detect concussions," January 2011.

[11] R. A. Potyrail, C. Surman, G. Steven, Y. Lee, T. Sivavec, and W. G. Morris, "Development of radio-frequency identification sensors based on organic electronic sensing materials for selective detection of toxic vapors," *Journal of Applied Physics*, vol. 106, pp. 124 902–1–124 902–6, December 2009.

[12] J. R. Smith, A. P. Sample, P. S. Powledge, S. Roy, and A. Mamishev, "A wirelessly powered platform for sensing and computation," in *Proceedings of the International Conference on Ubiquitous Computing*, 17 - 21 September 2006, pp. 495 – 506.

[13] G. A. Koo, "Signal constellation of a retrodirective array phase modulator," May 2011.

[14] J. T. Prothro, "Improved performance of a radio frequency identification tag antenna on a metal ground plane," May 2007.

[15] Analog Devices, "ADXL 345, 3-axis digital accelerometer," January 2011.

[16] Invensense, "IMU-3000, Motion Processing Unit," January 2011.

[17] G. L. Stuber, *Priciple of Mobile Communication.* U.S.: Springer, 2011.

[18] John G. Proakis and Massoud Salehi, *Digital Communications.* U.S.: McGraw-Hill Science/Engineering/Math, November, 2007.

[19] Thomas Starr, John M. Cioffi, and Peter J. Silverman, *Understanding Digital Subscriber Line Technology.* U.S.: Prentice Hall, January 1999.

[20] Jerry D. Gibson, *The Mobile Communications Handbook.* U.S.: CRC Press, February, 1999.

[21] Texas Instruments, "MSP430x2xx Family User Guide," January 2012.

[22] R. Hasse, V. Demir, W. Hunsicker, D. Kajfez, and A. Elsherbeni, "Design and analysis of partitioned square loop antennas," *Applied Computational Electromagnetics Society*, vol. 23, no. 1, pp. 53–61, March 2008.

[23] Constantine A. Balanis, *Antenna Theory: Analysis and Design.* U.S.: Wiley-Interscience, 2010.

[24] John Volakis, *Antenna Engineering Handbook.* U.S.: McGraw-Hill, 2007.

[25] The Isola Group, "Dk-Df Data."

[26] M. Abbak and I. Tekin, "Rfid coverage extension using microstrip-patch antenna array [wireless corner]," *Antennas and Propagation Magazine, IEEE*, vol. 51, no. 1, pp. 185 –191, feb. 2009.

[27] G. Seigneuret, T. Deleruyelle, E. Bergeret, and P. Pannier, "Backscattering optimization on rfid tags with multiple rf ports," in *Wireless Information Technology and Systems (ICWITS), 2010 IEEE International Conference on*, September 2010, pp. 1 –4.

[28] P. Nikitin and K. Rao, "Performance of rfid tags with multiple rf ports," in *Antennas and Propagation Society International Symposium, 2007 IEEE*, June 2007, pp. 5459 –5462.

[29] J. Griffin and G. Durgin, "Multipath fading measurements at 5.8ghz for backscatter tags with multiple antennas," *Antennas and Propagation, IEEE Transactions on*, vol. 58, no. 11, pp. 3693–3700, November 2010.

[30] J. Landt, "The history of rfid," *Potentials, IEEE*, vol. 24, no. 4, pp. 8–11, October–November 2005.

[31] R. Miesen, F. Kirsch, and M. Vossiek, "Holographic localization of passive uhf rfid transponders," in *RFID (RFID), 2011 IEEE International Conference on*, April 2011, pp. 32–37.

[32] P. Gulden, S. Roehr, and M. Christmann, "An overview of wireless local positioning system configurations," in *Wireless Sensing, Local Positioning, and RFID, 2009. IMWS 2009. IEEE MTT-S International Microwave Workshop on*, September 2009, pp. 1–4.

[33] J. Heidrich, D. Brenk, J. Essel, G. Fischer, R. Weigel, and S. Schwarzer, "Local positioning with passive uhf rfid transponders," in *Wireless Sensing, Local Positioning, and RFID, 2009. IMWS 2009. IEEE MTT-S International Microwave Workshop on*, September 2009, pp. 1–4.

[34] C. Hekimian-Williams, B. Grant, X. Liu, Z. Zhang, and P. Kumar, "Accurate localization of rfid tags using phase difference," in *RFID, 2010 IEEE International Conference on*, April 2010, pp. 89–96.

[35] P. Nikitin, R. Martinez, S. Ramamurthy, H. Leland, G. Spiess, and K. Rao, "Phase based spatial identification of uhf rfid tags," in *RFID, 2010 IEEE International Conference on*, April 2010, pp. 102–109.

[36] M. Algrain and J. Quinn, "Accelerometer based line-of-sight stabilization approach for pointing and tracking systems," in *Control Applications, 1993., Second IEEE Conference on*, vol. 1, September 1993, pp. 159–163.

[37] Apple Inc, "www.apple.com."

[38] R. Barbieri, E. Farella, L. Benini, B. Ricco, and A. Acquaviva, "A low-power motion capture system with integrated accelerometers [gesture recognition applications]," in *Consumer Communications and Networking Conference, 2004. CCNC 2004. First IEEE*, January 2004, pp. 418–423.

[39] X. Yun, E. Bachmann, A. Kavousanos-Kavousanakis, F. Yildiz, and R. McGhee, "Design and implementation of the marg human body motion tracking system," in *Intelligent Robots and Systems, 2004. (IROS 2004). Proceedings. 2004 IEEE/RSJ International Conference on*, vol. 1, September-October 2004, pp. 625–630.

[40] X. Yun and E. Bachmann, "Design, implementation, and experimental results of a quaternion-based kalman filter for human body motion tracking," *Robotics, IEEE Transactions on*, vol. 22, no. 6, pp. 1216–1227, December 2006.

[41] J. D. Jackson, D. W. Callahan, and P. F. Wang, "'location tracking of test vehicles using accelerometers," in *CSECS'06 Proceedings of the 5th WSEAS International Conference on Circuits, Systems, Electronics, Control and Signal Processing*, vol. 1, 2006, pp. 333–336.

[42] S. Cho and C. Park, "Mems based pedestrian navigation systems," *The Journal of Navigation*, vol. 59, pp. 135–153, 2006.

[43] W. Chen, R. Chen, Y. Chen, H. Kuusniemi, and J. Wang, "An effective pedestrian dead reckoning algorithm using a unified heading error model," in *Position Location and Navigation Symposium (PLANS), 2010 IEEE/ION*, May 2010, pp. 340–347.

[44] Sparkfun Electronics, "www.sparkfun.com."